ASTROBIOLOGY
Volume 18, Number 4, 2018

DOI: 10.1089/ast.2017.1716

Research Article

Detecting Kerogen as a Biosignature Using Colocated UV Time-Gated Raman and Fluorescence Spectroscopy

Svetlana Shkolyar,[1,2*] Evan J. Eshelman,[3] Jack D. Farmer,[1] David Hamilton,[3] Michael G. Daly,[3] and Cody Youngbull[4]

Abstract

The Mars 2020 mission will analyze samples *in situ* and identify any that could have preserved biosignatures in ancient habitable environments for later return to Earth. Highest priority targeted samples include aqueously formed sedimentary lithologies. On Earth, such lithologies can contain fossil biosignatures as aromatic carbon (kerogen). In this study, we analyzed nonextracted kerogen in a diverse suite of natural, complex samples using colocated UV excitation (266 nm) time-gated (UV-TG) Raman and laser-induced fluorescence spectroscopies. We interrogated kerogen and its host matrix in samples to (1) explore the capabilities of UV-TG Raman and fluorescence spectroscopies for detecting kerogen in high-priority targets in the search for possible biosignatures on Mars; (2) assess the effectiveness of time gating and UV laser wavelength in reducing fluorescence in Raman spectra; and (3) identify sample-specific issues that could challenge rover-based identifications of kerogen using UV-TG Raman spectroscopy. We found that ungated UV Raman spectroscopy is suited to identify diagnostic kerogen Raman bands without interfering fluorescence and that UV fluorescence spectroscopy is suited to identify kerogen. These results highlight the value of combining colocated Raman and fluorescence spectroscopies, similar to those obtainable by SHERLOC on Mars 2020, to strengthen the confidence of kerogen detection as a potential biosignature in complex natural samples. Key Words: Raman spectroscopy—Laser-induced fluorescence spectroscopy—Mars Sample Return—Mars 2020 mission—Kerogen—Biosignatures. Astrobiology 18, 431–453.

1. Introduction

1.1. Searching for biosignatures in martian samples

The 2011 Planetary Science Decadal Survey (National Research Council, NRC, 2011) and the 2008 NASA Astrobiology Roadmap (Des Marais *et al*., 2008) assign a high priority to searching for past or present life on Mars. Both documents recommend that the highest priority for the coming decade should be to send a mission to Mars to cache a suite of samples containing potential signatures of past or present life for later biogenicity analysis on Earth using multiple lines of evidence from sophisticated laboratory tools (NanoSIMS for isotopic and elemental distributions, X-ray absorption near edge structure spectroscopy for carbon bonding and structural information, etc.). As a first step toward this goal, NASA's Mars 2020 rover will use a defined instrument suite to select and cache $\sim$30 g of samples with a total mass of <500 g (Mustard *et al*., 2013).

To meet mission goals, there is a need to assess the ability of *in situ* techniques selected for the instrument payload to identify the best samples through realistic terrestrial analog studies. To maximize the chances of finding biosignatures in collected samples, it is crucial to develop a strategy for *in situ* selection of samples, based on their contextual association with past habitable environments and potential to preserve biosignatures (Farmer and Des Marais, 1999; Farmer, 2012).

The largest pool of organic matter on Earth is sedimentary reduced organic carbon (Farmer and Des Marais, 1999). After burial, this carbon undergoes degradation (*e.g.*, thermal maturation) and alteration into complex mixtures of macromolecular amorphous and aromatic carbon, primarily as polycyclic aromatic hydrocarbons (PAHs), known as kerogen. The initial composition, structure, and thermal maturation pathway will define the aromaticity and final makeup of the kerogen. For example, low thermal maturity kerogen is typically composed of long chain aliphatic

[1]School of Earth and Space Exploration, Arizona State University, Tempe, Arizona.
[2*]Current address: Geophysical Laboratory, Carnegie Institution of Washington, Washington, District of Columbia.
[3]The Centre for Research in Earth and Space Science (CRESS), York University, Toronto, Ontario, Canada.
[4]Flathead Lake Biological Station, University of Montana, Polson, Montana.

hydrocarbons. See Marshall *et al.* (2010) for a review of how terrestrial organic matter matures to kerogen. On Earth, kerogen represents $\sim 10^{16}$ tons of C compared with $\sim 10^{12}$ tons as living biomass (Vandenbroucke and Largeau, 2007).

Although there are nonbiological sources for kerogen (Section 1.2), given biogenic kerogen's abundance on Earth, one might expect it to be the likeliest biosignature detectable in solid samples on Mars (although Mars 2020 instruments will search for organics from other biosignature sources as well).

Terrestrial kerogen is commonly captured and preserved in aqueous lithologies, such as silica (chert), carbonates, sulfates, and mudstones, all of which have been detected on Mars. Chert is a dense, highly silicified, fine-grained sedimentary rock, whose dense crystalline structure resists chemical weathering (McIlreath and Morrow, 1990). Its prolonged residence time in the crust makes it one of the most common lithotypes in which microbiota are preserved in the Precambrian record on Earth (Farmer and Des Marais, 1999). Chert, its precursor opaline silica, and a low-pressure, high-temperature polymorph, tridymite, have all been detected recently at Mars rover landing sites (Skok *et al.*, 2010; Ruff *et al.*, 2011; Morris *et al.*, 2016).

Carbonates such as calcite ($CaCO_3$) and magnesite ($MgCO_3$) are also common host minerals for Earth's Precambrian fossil record (Farmer and Des Marais, 1999). Carbonates have been detected on Mars both from orbit (Ehlmann *et al.*, 2008b) and from the surface (Madden *et al.*, 2004; Morris *et al.*, 2010).

Gypsum ($CaSO_4 \cdot H_2O$), another common lithotype for preserving kerogenous microfossils, is considered a promising target in the search for past life on Mars (Schopf *et al.*, 2012). Gypsum and other hydrated sulfates have been observed both from orbit (Bibring *et al.*, 2006; Glotch and Rogers, 2007) and *in situ* (Squyres *et al.*, 2004, 2012; Glotch *et al.*, 2006) as components of soils and evaporite deposits.

Fine-grained mudstones, particularly those that contain hydrated aluminum phyllosilicates (clays), have a high potential for capturing and preserving organic matter (Farmer and Des Marais, 1999; Ehlmann *et al.*, 2008a). On Earth, organic compounds adsorb as molecular monolayers on clay surfaces. Clays, including smectites, have been identified on Mars from orbit (Ehlmann *et al.*, 2008a; Noe Dobrea *et al.*, 2012) and by the Mars Science Laboratory rover (Vaniman *et al.*, 2014; Bristow *et al.*, 2015). Furthermore, all of these lithotypes have been identified in martian meteorites (Bridges and Grady, 2000; Bridges *et al.*, 2001; Steele *et al.*, 2007, 2012a, 2012b).

The above lithotypes have long been considered high-priority targets in the search for a martian fossil record (Farmer and Des Marais, 1999; Schopf *et al.*, 2012) if such a record exists. Kerogen has not been detected on Mars, but it exemplifies one possible biosignature to search for at the landing site selected for Mars 2020. For this study, we selected seven diverse terrestrial samples (Table 1) that make up some of the most common lithotypes on Earth to preserve kerogen. These samples were analyzed with UV time-gated (UV-TG) Raman and fluorescence spectroscopies.

1.2. Biosignature searches with Raman spectroscopy

Raman spectroscopy was selected for Mars 2020 to identify potential biosignatures and their mineral context *in situ* to help inform decisions in selecting samples for caching. Raman spectroscopy is a light-scattering, vibrational spectroscopy technique that is well suited for this task. First, it allows the identification of both organic and inorganic compounds (including minerals), even when present together. Second, unlike similar *in situ* techniques, Raman spectroscopy is not destructive to samples (with low laser energy density). In addition, the technique requires no sample preparation, although surface grinding (*e.g.*, using the Rock Abrasion Tool; Gorevan *et al.*, 2003) optimizes the Raman signal by reducing sample topography as well as removing surface weathering rinds.

In a Raman spectrum, kerogen is identified by two bands that represent the vibrational modes of macromolecular sp^2 carbon, whether or not they are biogenic. With visible laser wavelength excitation (λ_{ex}), these spectral features consist of a D band, or disordered lattice stretching mode of aromatic carbon at $\sim 1350\,cm^{-1}$, and an in-plane C=C stretching mode, the G band, present between 1560 and $\sim 1600\,cm^{-1}$ (Ferrari and Robertson, 2001; Pasteris and Wopenka, 2003; Marshall *et al.*, 2010).

Additional features of lower intensity may also be present at ~ 2450, ~ 2695, ~ 2735, ~ 2920–2940, and $\sim 3248\,cm^{-1}$, representing second-order modes of first-order bands that result from overtone or combination scattering, structural ordering, and potential C-H stretching modes associated with kerogen and carbon (Pasteris and Wopenka, 2003; Ferrari and Robertson, 2004; Czaja *et al.*, 2009; Marshall *et al.*, 2010). D and G bands can be a convolution of multiple additional bands (Czaja *et al.*, 2009; Marshall *et al.*, 2010).

When interrogated with UV λ_{ex}, these compounds display slightly different Raman vibrational modes due to enhanced cross sections of these organic vibrational modes (Section 1.3). With UV λ_{ex}, the region between 1100 and $1500\,cm^{-1}$ can consist of many convolved bands, attributable to C=C ''breathing modes'' in ringed structures such as PAHs, sometimes interlinked by polyene chains (Czaja *et al.*, 2009; Abbey *et al.*, 2017). In the UV, the D band (which can peak between 1296 and $1401\,cm^{-1}$; Abbey *et al.*, 2017) arises only when sp^2 carbon sites are in disordered rings and is absent when those sites are highly graphitic or present in chains of rings (Ferrari and Robertson, 2001).

Raman spectroscopy has long been used to assess the biogenicity of organic and inorganic materials. For example, extant endolithic biomarkers (Dickensheets *et al.*, 2000; Jorge-Villar and Edwards, 2013 and references therein), putative kerogenous microfossils in ~ 3.5 Ga cherts (Brasier *et al.*, 2002; Schopf *et al.*, 2002; Marshall *et al.*, 2011), and graphitic carbon in ~ 3.87 Ga samples (Papineau *et al.*, 2011; Bell *et al.*, 2015) have been examined by using Raman spectroscopy with laser excitation wavelengths between 488 and 1064 nm. Raman spectroscopy has also been used, with 532 nm laser excitation, to identify D and G bands in abiotic macromolecular carbon (MMC) in many martian meteorites (Steele *et al.*, 2012a, 2012b, 2016).

These analyses emphasize that the use of Raman spectroscopy for the detection of D or G bands of biogenic kerogen can be similar to its use for the detection of those of disordered, nonbiogenic MMC, and therefore, Raman detections of D and G bands alone do not establish biogenicity (Brasier *et al.*, 2002; Pasteris and Wopenka, 2003; Marshall *et al.*, 2010; Bower *et al.*, 2013).

By extension, on Mars, the detection of D and G bands in a Raman spectrum would be evidence of aromatic carbon, but

Table 1. Sample Ages, Localities, and Phases Detected by Characterization Techniques: Reflected or Transmitted Microscopy (M), Visible Continuous Wave Raman (V), and X-Ray Powder Diffraction (X)

Sample	*Approximate age*	*Locality*	*Component*
Hydrothermal chert	<3.43 BYA (Lowe, 1980)	Strelley Pool Formation, Pilbara, Australia	**Quartz (M, V, X)** Dolomite (M, V) Pyrite[a] (M) Alunite[a] (M) Kerogen (M, V)
Silicified shale	≤65 MYA (Moore, 1979)	Gerlach, NV	**Quartz (M, V, X)** Pyrite (M, V) Sphalerite (M, V, X) Kerogen (M, V)
Marine sandstone	~490 to 488 MYA (Muller *et al*., 2009)	Alum Formation, Öland, Sweden	**Quartz** (M, X) Plagioclase Feldspar (M, X) Dolomite (V) **Calcite (M, X)** Pyrite (M, V, X) Glauconite (M, V) Muscovite/Phlogopite Mica (M, V) Illite (M, X) Kerogen (M, V)
Sulfate evaporite	300–250 MYA (Anderson *et al*., 1972)	Castile Formation, Delaware Basin, TX	**Gypsum (M, V, X)** Dolomite (M, V) **Calcite (M, X, V)** Anhydrite (M, V) Sylvite (X) Kerogen (M, V)
Stromatolitic limestone	<10,000 YA (Osborne *et al*., 1982)	Walker Lake, NV	**Calcite (M, V, X)** Dolomite (V) Quartz (M, V, X) Plagioclase Feldspar (sodic) (M, V, X) Kerogen (M, V)
Lacustrine carbonate	~56–34 MYA (Surdam and Stanley, 1979)	Green River, WY	**Calcite (M, V, X)** Dolomite (X) Volcanic ash[a] (M) Kerogen (M, V)
Evaporitic mudstone	7.5–2.5 MYA (Bressler and Butler, 1978)	Verde Basin, AZ	**Magnesite (M, X)** Na, Ca, and K Feldspars (M, V) Quartz (M, V, X) Gypsum (M, V, X) Thenardite (M, V, X) Glauberite (M, V) Arzakite (M, V) Hematite (M, V) Other iron oxides[b] (M, V) **Muscovite (M, V, X)** **Montmorillonite (X)** **Fe, Mg Saponite (X)** Kerogen[a] (M)

Bolded phases indicate the most abundant phase and also the main kerogen preservation phase.
[a]Phases suspected based on microscopy observations whose definitive identities remain unconfirmed by other techniques.
[b]Visible to near infrared reflectance spectroscopy confirmed the presence of hematite, goethite, and lepidocrocite after microscopy suggested their presence (Shkolyar and Farmer, in revision) but did not provide abundances.

it would not distinguish biogenic kerogen from abiotic MMC. Instead, it would indicate a compelling potential biosignature and favor sample caching. After Earth return, detailed chemical and biogenicity analyses would be needed.

To make the best caching decisions, it will be essential to understand the geological (*e.g.*, microtextural and geochemical) context in which organics are preserved, a primary recommendation of the Mars 2020 Science Definition Team (Mustard *et al*., 2013). Raman spectroscopy can provide this needed context, particularly when combined with microscale imaging and fluorescence spectroscopy, as demonstrated in this study.

1.3. Fluorescence in the Raman spectrum

Raman spectroscopy is challenged by interfering background fluorescence, a type of luminescence often several

orders of magnitude stronger than the Raman scattering signal. Fluorescence occurs when an incident photon is absorbed by a molecule or species, exciting it to a higher electronic state. The molecule then relaxes back to the ground state, emitting a photon. Many minerals and organics exhibit fluorescence that can conceal their Raman signatures. Background fluorescence has been shown to hamper the identification of minerals (Bartholomew, 2012), kerogen and its components (Marshall *et al*., 2006, 2010; Schopf *et al*., 2012), and other biosignatures targeted for Mars (Dickensheets *et al*., 2000), both in the laboratory and when using field-deployed Raman systems (Jehlicka *et al*., 2010).

Furthermore, the design of Raman systems does not often engage the challenges of natural geological materials (*e.g.*, Bartholomew, 2012, 2014). In prioritizing samples for Mars Sample Return (MSR) based on Raman spectra, false negative conclusions about the value of a sample for caching may occur if collected background fluorescence hides relevant Raman bands that indicate potential biosignatures (*e.g.*, those described in Section 1.2).

Strategies to mitigate fluorescence signals in Raman spectra include (1) tuning the excitation wavelength to the UV, where it is in resonance with the targeted substance (Asher, 1993; Frosch *et al*., 2007), (2) using a confocal Raman setup (Brasier *et al*., 2002; Schopf *et al*., 2002; Fries and Steele, 2010; Bower *et al*., 2016), (3) using shifted-excitation Raman difference system (Shreve *et al*., 1992), or (4) using time-gated Raman spectroscopy. Here, we explore time gating and UV excitation.

Time gating uses pulsed laser excitation and gated detection (*i.e.*, detection of only those photons scattered or emitted in temporal proximity to the laser pulse) to capture the instantaneous Raman-scattered photons and ''gate out'' (exclude) the longer lifetime fluorescence signal in the time domain (Fig. 1; Martyshkin *et al*., 2004; Gaft and Nagli, 2009). In contrast, with continuous wave (CW) Raman spectroscopy, the laser continuously irradiates the sample without laser pulsing or gating.

Another fluorescence reduction strategy explored here is the λ_{ex} in the UV, which has two advantages. First, a UV λ_{ex} causes Raman and fluorescence signals to become energetically separated (Tarcea *et al*., 2007). Second, depending on the wavelength and targeted compound, a UV λ_{ex} can induce resonance within electronic bands of certain classes of organics (Hug *et al*., 2005; Marshall *et al*., 2010 and references therein), including complex organics such as kerogen (Czaja *et al*., 2009). Resonances can increase scattering efficiency by orders of magnitude, allowing organic detection limits from ppm (Beegle *et al*., 2015; Abbey *et al*., 2017) to ppb levels (Storrie-Lombardi *et al*., 2001). However, this also means that signals from trace organic contaminants on the surface, which may have a similar structure to kerogen (*i.e.*, containing PAHs), can also be amplified (Ray *et al*., 2000; Ferrari and Robertson, 2001).

1.4. Fluorescence spectroscopy

Fluorescence can provide useful information when a dedicated spectrometer collects laser-induced fluorescence spectra. Collected in this way, the fluorescence phenomenon can be used to one's advantage in organic analysis. When examined in the temporal domain, the fluorescence intensity $I(t)$ decays over time t as $I(t)=I_0\ e^{-t/\tau}$, where decay lifetimes, τ (which represents the time a fluorophore will remain in an excited state), can help determine whether fluorescence originates from inorganic or organic sources (Fig. 1).

Fluorescence originating from inorganic sources, such as lattice defects, trace metals, or rare-Earth impurities, typically has a $\tau > 1$ µs, whereas fluorescence originating from organic fluorophores typically has $\tau \lesssim 100$ ns (Sharma *et al*., 2003; Bozlee *et al*., 2005; Misra *et al*., 2016). Kerogen biogenicity cannot be definitively established with Raman spectroscopy alone (Pasteris and Wopenka, 2003; Marshall *et al*., 2010), but colocated gated UV Raman and fluorescence data sets can be obtained on a microscale location on a sample, where kerogen candidates have been previously targeted with imaging analyses, as done here, to enhance the confidence of kerogen identification.

1.5. Raman spectroscopy on Mars rovers

To date, neither Raman nor laser-induced fluorescence spectroscopy instruments have flown on a space mission.

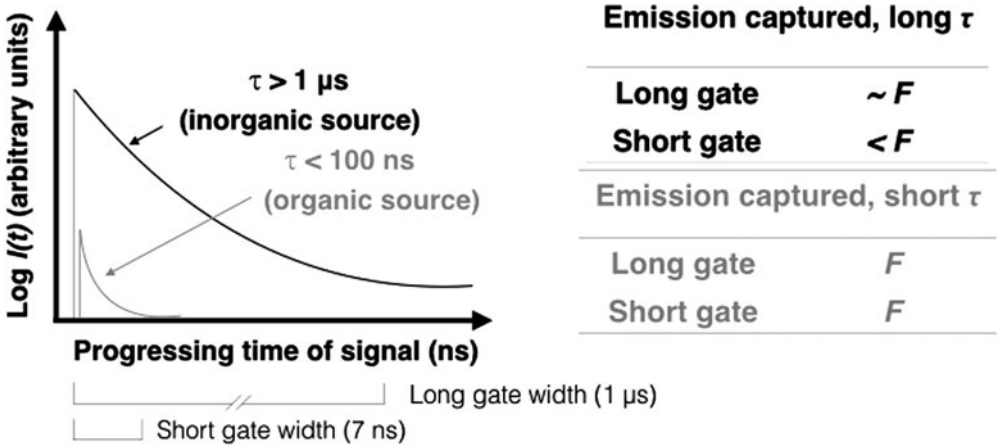

FIG. 1. Principles of time-resolved fluorescence. Fluorescence emission $I(t)$ decays exponentially for a single excited state. F is the arbitrary fluorescence emission of a sample after interaction with one laser pulse, shown as a function of detector time gate width. Inorganic materials emit long-lifetime (τ) fluorescence (black curve); a long gate captures almost the full emission ($\sim F$), but a shorter gate captures less than the full emission ($<F$). Organics emit short τ fluorescence (gray curve); both long and short gates would capture the majority of a signal (F). The gate widths shown are those used in our experimental setup.

The Mars 2020 rover will include two of the first flown Raman and fluorescence instruments to identify and cache samples containing potential organic biosignatures. One is the Scanning Habitable Environments with Raman & Luminescence for Organics & Chemicals (SHERLOC), an arm-mounted resonance Raman (810 to >3600 cm^{-1}) and fluorescence (250–360 nm) spectrometer, with a deep-UV 248.6 nm pulsed laser source (Beegle *et al*., 2015). The other is SuperCam, an integrated suite of four instruments that include a stand-off spectrometer and a microimager. SuperCam will have a pulsed laser with time-gated ($\lesssim$100 ns) excitation at 532 nm for Raman (50–4400 cm^{-1}) and fluorescence (534–850 nm) measurements (Clegg *et al*., 2015).

Although this study aims to inform data interpretations that may be made with SHERLOC, there are many differences between our UV Raman and fluorescence system and SHERLOC (*e.g.*, spot sizes, spatial and spectral resolutions, and fluorescence collection ranges).

Another Raman system is being planned for ExoMars, which is a European Space Agency rover also planned to launch in 2020. The ExoMars Raman laser spectrometer is planned to be the first CW 532-nm Raman system flown and will be designed to perform *in situ* analyses to search for potential biosignatures (Bost *et al*., 2015), if any are detected and analyzed.

1.6. Objectives of this study

The rapidly approaching Mars 2020 mission brings about a crucial need to better understand the capabilities of Raman and fluorescence instruments to identify biosignatures in realistic, natural, and complex Mars analog samples. Recent work has demonstrated the capabilities of UV Raman and fluorescence instruments for biosignature detection on Mars (*e.g.*, Smith *et al*., 2014), including those that form the foundation of the SHERLOC instrument (Beegle *et al*., 2014, 2015, 2016; Abbey *et al*., 2017) and the foundation of the UV system used here (Eshelman *et al*., 2014, 2015; Skulinova *et al*., 2014). However, these previous studies investigated synthetic, pure, or extracted and concentrated organics, or mineral powders spiked with organic molecules, and they do not take into account complex interactions of mixed-phase, fossilized organics interacting with their host matrix, as found in nature.

Others have examined natural, although extant and labile biosignatures, with Raman spectroscopy (*e.g.*, Dickensheets *et al*., 2000; Jorge-Villar and Edwards, 2013) and UV time-resolved fluorescence techniques (*e.g.*, Misra *et al*., 2016). However, surface conditions on Mars are unlikely to support extant life. Evidence for past life, if it existed, will likely be found as fossilized biosignatures in ancient sedimentary rocks as is the case for the record of life preserved in Precambrian rocks on Earth (Farmer and Des Marais, 1999). The Mars 2020 rover payload may have the best chances of encountering and analyzing biosignatures found as fossilized, complex, macromolecular compounds preserved within a host mineral (as detailed in Section 1.1).

In this study, we explored biosignature detection strategies using UV-TG Raman and fluorescence instruments that produce data sets on nonextracted, naturally preserved kerogen in a diverse suite of challenging field-collected samples similar to rock types targeted in the search for a potential martian fossil record, if one exists (Section 1.1). Here, we analyze a suite of such samples (Table 1) using a nanosecond-pulsed, combined UV Raman and fluorescence system. Our study goals were to:

(1) explore the capabilities of UV-TG Raman and fluorescence spectroscopies for detecting naturally preserved kerogen in well-characterized, complex samples;
(2) assess the effectiveness of time gating and UV laser λ_{ex} in reducing fluorescence in Raman spectra of kerogen and host minerals; and
(3) identify sample-specific issues that could challenge rover-based identifications of kerogen using UV Raman spectroscopy.

2. Materials and Methods

Seven samples were selected to represent a broad range of depositional environments, ages, and diagenetic histories. Sample collection localities, ages, and compositions are summarized in Table 1. All samples contained natural, nonextracted kerogen of diverse maturities and modes of preservation within host rock matrices, and exhibited diverse ranges of fluorescence.

Samples included a hydrothermal chert, silicified shale, carbonate-cemented marine sandstone, laminated sulfate–carbonate evaporite, lacustrine stromatolitic limestone, lacustrine micritic carbonate, and clay- and magnesite-rich evaporitic mudstone. Each sample was prepared as petrographic thin sections (for light microscopy and visible Raman spectroscopy), powders (for X-ray powder diffraction [XRPD]), and rock chips (for UV-TG Raman/fluorescence spectroscopy).

All samples were first characterized with microscopy, visible CW Raman spectroscopy, and XRPD. Next, spatially colocated UV-TG Raman and fluorescence spectra were obtained on the same candidate kerogen grains (precisely targeted with microscopic imaging) and mineral matrix regions, as SHERLOC may do on Mars (Beegle *et al*., 2015). See Supplementary Fig. S1 (Supplementary Data are available at http://online.liebertpub.com/suppl/doi/10.1089/ast.2017.1716) for a flowchart of sample preparation methods and analyses.

2.1. Petrographic microscopy

Thin section microscopy was undertaken to understand microtextures, diagenesis (postdepositional alteration processes), and mineralogy of samples (and was subsequently confirmed by other techniques). Sample paragenesis (time-ordered sequence of environmental processes and temporal relationships among phases) was also reconstructed. Thin sections were imaged with a Nikon Eclipse E600 POL polarizing light microscope and an Optronix camera system. Photomicrographs of representative areas of interest in each sample were obtained under transmitted (plane-polarized and cross-polarized) and reflected light. Standard (30-μm thick) uncovered petrographic thin sections of all samples were vacuum embedded in epoxy (nonfluorescent EPOTEK 301). Thin sections were prepared by Spectrum Petrographics, Inc.

One inch rock chips were obtained by breaking off chunks from larger samples to expose fresh interior surfaces. Chips could only be imaged under reflected light for UV-TG Raman and fluorescence analyses.

For preliminary identifications, we searched for candidate kerogen grains ($\sim$10s of microns in size) in regions likely to preserve kerogen (*e.g.*, darker laminae where kerogen is often

concentrated; Section 3). Alternating between optical illumination settings (plane- vs. cross-polarized light; transmitted vs. reflected light) was necessary to identify candidate kerogen grains (*e.g.*, kerogen and Fe oxides are opaque in plane-polarized or cross-polarized light, but Fe oxides are distinguishable based on their reflectivity in reflected light).

Markers were adhered onto thin section and rock chip surfaces to indicate the precise locations of targeted kerogen as well as mineral regions for further analyses. This marker approach allowed us to successfully locate the same microscale features for Raman spectroscopy analyses. We then documented major and minor mineral components, representative microtextures, and cross-cutting relationships. Raman and XRPD were used to refine mineral identifications that were predicted by using microscopy.

2.2. Visible CW Raman spectroscopy

We used a visible CW Raman spectrometer at ASU's Center for Solid State Science to obtain point spectra of candidate kerogen grains and minerals *in situ*. This system is neither optimized for planetary applications nor intended to be compared with the UV Raman instrument described here. Rather, this system was used to understand the 532 nm laser-induced background fluorescence behavior of kerogen and its host matrix in preparation for UV-TG Raman analyses, with the understanding that Raman and fluorescence signals overlap in the visible and become energetically separated with UV λ_{ex} (Tarcea *et al*., 2007).

This CW Raman system comprises a 532 nm Coherent Sapphire SF laser source and a Princeton Instruments liquid nitrogen cooled charge-coupled device (CCD) detector and Acton 300i spectrograph. The laser was focused onto the sample by using a 50X APO Mitutoyo objective. The Raman signal was collected through an Acton 300i spectrograph (1200 lines/mm grating) onto a Princeton Instruments liquid nitrogen cooled CCD. The system had a spectral resolution of $\sim 2\,cm^{-1}$, spatial resolution of $\sim 0.5\,\mu m$, and an acquisition window from 70 to $2000\,cm^{-1}$.

Raman point spectra were acquired on previously targeted candidate kerogen grains and mineral matrices (Section 2.1). A built-in transmitted light microscope was used to locate previously targeted regions of interest (shown in Figs. 3–9 with the green laser spot on regions interrogated). The Raman laser spot (<5 μm diameter) was manually focused on the sample surface. Spectra were acquired over a range of integration times, power settings, and depths below the thin section surface to obtain spectra that minimized fluorescence and maximized signal to noise (S/N) ratios as well as spectral band visibility. Acquisitions ranged from one to twenty 10- to 15-s integrations at low energies of 0.75 to 6 mW power (or $\sim 7.6\times10^3$ to $\sim 6.1\times10^4$ W/cm^2) for each analysis (or higher where noted). Sampling depths were ~ 1 to 20 μm below thin section surfaces.

Raman shift positions were calibrated with a cyclohexane standard. No spectral postprocessing was applied to Raman spectra to highlight fluorescence contributions to the total signal. Minerals were identified with *CrystalSleuth* database (Downs, 2006).

For Raman analyses, care was taken to avoid contamination. Contamination could arise from thin section epoxy; however, no spectral features from epoxy were seen (Supplementary Fig. S2). Contamination arising from marker adhesive was mitigated by cleaning each thin section (but not rock chips) with 95% ethanol and distilled water. In addition, the micron-scale imaging resolution of the Raman optical imaging system allowed us to ensure that the laser spot did not overlap with the adhered markers.

2.3. Visible CW confocal Raman imaging spectroscopy

To elucidate the nature, size, and distribution of organics in one representative sample, we performed Raman imaging on the stromatolitic limestone sample chip (Fig. 6C–G).

For this analysis, we used a customized WITec α-scanning near-field optical microscope incorporating confocal Raman spectroscopic imaging, because it provides exceptional spatial (micrometer scale) and spectral resolution (Bower *et al*., 2016) and reduces the much more intense fluorescence signal through the confocal optics used (Fries and Steele, 2010). This instrument is capable of collecting either single spectra or 2D micro-Raman maps. Maps of organic distributions on the stromatolite surface were generated by using a frequency-doubled solid-state YAG laser (532 nm) operating at 0.01–5 mW output power through a 600 lines/mm grating onto an Andor EMCCD chip. Spectra (with an acquisition range from 0 to $3600\,cm^{-1}$) were taken at each pixel with an integration time of 2 s per pixel at 3 μm step sizes. Data processing was performed with WITec Control Four 4.1 software.

2.4. X-ray powder diffraction

For XRPD analyses, bulk powdered samples were obtained for each sample for confirmation of mineralogy determined by the mentioned analyses. (Kerogen cannot be identified with XRPD.) Bulk sample fractions were chipped, crushed, ground with a quartz mortar and pestle, and sieved to <150 μm. A Siemens D5000 X-ray Diffractometer with a Ni-filtered Cu radiation source was used to identify minerals in bulk sample powders. Powders were scanned from 5° to 81.759° with a step size of 0.016°. Operating conditions were 40 kV at 30 mA using CuKα ($\lambda_{\alpha1} = 1.5060$ Å; $\lambda_{\alpha2} = 1.54439$ Å) with an 8-s dwell time, for an analysis time of 12 h per sample. Background subtraction and mineral identifications were performed with the *JADE*™ version 9 (Materials Data, Inc.), with the International Centre for Diffraction Data database.

2.5. UV-TG Raman and fluorescence spectroscopies

UV radiation absorption by thin section components (glass slides and embedding epoxy) significantly weakens the Raman signal. Therefore, we used flat rock chips for UV-TG Raman and fluorescence analyses. Sample surfaces were ground flat with aluminum oxide abrasive paper (400 grit; Northon St. Gobain Premium) to reduce surface organic contamination for all but the hardest samples (chert and silicified shale). Microscopy confirmed that no abrasive paper contaminants were present on the ground sample surfaces. Abraded rock surfaces represent an analogous sample preparation to what will be possible on Mars when using a rock abrasion tool (Gorevan *et al*., 2003).

For each sample, four data sets were obtained on the same microscale spot in samples with pretargeted candidate kerogen grains and mineral matrix regions: (1) Raman spectrum, long gate (to mimic a nongated, CW 266 nm Raman system);

Raman spectrum, short gate (to assess the effectiveness of gating for fluorescence reduction); (3) fluorescence spectrum, long gate; and (4) fluorescence spectrum, short gate.

Short and long gate widths were 7 ns and 1 μs, respectively, determined by using a powdered gypsum tablet standard. Even though organic fluorescence can take up to 100 ns to decay (Fig. 1), we chose a short gate of 7 ns to discriminate between organic and mineral fluorescence; in our samples, the majority of the long-lived fluorescence was rejected and most short-lived fluorescence was emitted in the first 7 ns (Fig. 11B, F). A gate delay (which coordinates opening the gate with the arrival of the laser pulse by applying an electronic delay after receiving the external trigger signal; Eshelman *et al*., 2015) of 2 ns was applied to short gate measurements. A total of 12,000 accumulations were acquired for all data with an exposure time (when the CCD is exposed while pulses are accumulated) of 0.05 s.

For each acquisition, a background spectrum (with the input from the laser to the sample blocked) was acquired, followed by an alanine standard for calibration, and then point spectra of regions in each sample.

Spectra were obtained with a pulsed, 266 nm laser wavelength excitation Raman combined with a laser-induced fluorescence system with a gated, intensified CCD detector. The laser spot size was $\sim 25 \times \sim 35$ μm. A flat field correction was performed with an NIST deuterium lamp standard to remove CCD and edge filter irregularities. Raman spectra were acquired with a 2400 lines/mm grating, allowing a spectral range of 286–3805 cm^{-1}. For fluorescence measurements, the Raman spectrometer grating was interchanged with a 300 lines/mm grating, allowing an acquisition range of 268–528 nm. The laser was pulsed at 5 kHz with a pulse energy of 1.6 μJ, resulting in a fluence of ~ 0.2 J/cm^2 (2.3×10^5 W/cm^2). Other system details were provided by Eshelman *et al*. (2015). No postprocessing was applied to Raman spectra to highlight the low fluorescence contributions to the total signal.

To quantify the effect of gating on fluorescence reduction with UV-TG Raman spectroscopy, we obtained time-resolved fluorescence spectra and associated fluorescence decay curves of selected samples. (See Section 3.9 and Fig. 11 for details.) Fluorescence spectra were obtained at increasing gate delays by accumulating a fluorescence signal and incrementing the gate delay by 0.1 ns steps. This allowed spectra to be obtained in the intensity I, time t, and wavelength λ domains. Spectra were acquired with a gate width of 3 ns, 40 accumulations per spectrum, and an exposure time of 0.05 s.

All data sets were also acquired on the following mineral standards (without sterile handling): synthetic silica sand (Barco 49, 99.7% SiO_2), natural gypsum (Sigma Aldrich lot #SLBC4109V), natural dolomite (Wards research grade 49-5871 Selasvann, Norway), and natural calcite (Wards research grade, 49-5860 Chihuahua, Mexico). For a kerogen standard, 1 mg of extracted natural kerogen (94% carbon) was obtained, courtesy of R. Summons and E. Matys (Massachusetts Institute of Technology).

3. Results

3.1. Archean hydrothermal chert, Strelley Pool Formation, Pilbara, Australia

The Strelley Pool Formation is a stratiform limestone-chert sequence that hosts the oldest known coniform stromatolites likely deposited in a shallow marine environment during the Archaean (Lowe, 1980; Hofmann *et al*., 1999; Van Kranendonk *et al*., 2003; Allwood *et al*., 2006). Our sample was collected from a vein of black chert part of a younger dike system that cross cuts the Strelley Pool Formation at the Trendall locality.

Optical microscopy showed a quartz matrix surrounding abundant particulate grains, whose black color and absence of reflectivity are consistent with kerogen. These grains were found mostly within regions of microcrystalline (<20 μm grains) quartz; conversely, zones of coarser grained megaquartz (>20 μm grains) showed a lower abundance of those grains (Fig. 2A).

The presence of kerogen and quartz was confirmed by visible CW Raman spectroscopy: both were easily detectable due to the low overall fluorescence of this sample (Fig. 2B). Our average CW Raman D and G band positions (1345 and 1602 cm^{-1}) are consistent with those of Bower *et al*. (2013) who obtained similar average D and G band positions for abundant kerogen found in samples collected from the same locality (1342 and 1602 cm^{-1}). Our CW Raman data on this sample's kerogen are also consistent with Bower *et al*. (2013) and Allwood *et al*. (2006) who concluded that kerogen found in their Strelley Pool samples indicates high thermal maturity (Supplementary Fig. S3). Supplementary Fig. S4 also shows the CW Raman spectrum of this sample, where it can be seen stacked for comparison with the other less mature samples we studied. Other observed minor phases, with tentative identifications, are listed in Table 1.

3.2. Tertiary silicified shale, Wind Mt. Mine, Gerlach, Nevada

The Wind Mt. mine exposes a fine-grained silicified shale, which experienced intense geothermal activity associated with pervasive silicification and the emplacement of epithermal gold deposits (Wood, 1991; Eneva *et al*., 2011).

Microtextural analysis with microscopy revealed a fine-grained mudstone/shale matrix and microcrystalline quartz (Fig. 3A), consistent with an interpretation that quartz was a later-stage diagenetic replacement. Quartz was detected by using all techniques (Fig. 3; Table 1). Microscopy, along with Raman data, showed abundant dark opaque particulate grains within the quartz matrix (Figs. 3A and 4C) interpreted to be candidate kerogen regions, as well as morphologically distinct regions, suspected to be permineralized fossil plant fragments (Fig. 3B). In sample chips, light-colored kerogenous regions were preserved within gray-colored quartz (Fig. 10F). Sulfide minerals such as pyrite (FeS_2) were also identified with microscopy and CW Raman spectroscopy, often associated with kerogen (Fig. 3A, C, Table 1). In visible CW Raman spectra, kerogen and quartz displayed moderate fluorescence (Fig. 3C).

3.3. Upper Cambrian carbonate-cemented marine sandstone, Alum Formation, Öland, Sweden

This sample was collected from a shale interbed within a carbonate-cemented, quartzo-feldspathic sandstone of the Upper Cambrian Alum Formation (Table 1; Maeda *et al*., 2011).

Microscopy and Raman analyses revealed dolomite cement and phyllosilicates (*e.g.*, platy micas; Table 1), sometimes deformed (Fig. 4A), probably by compaction, and often associated with abundant, often large kerogen

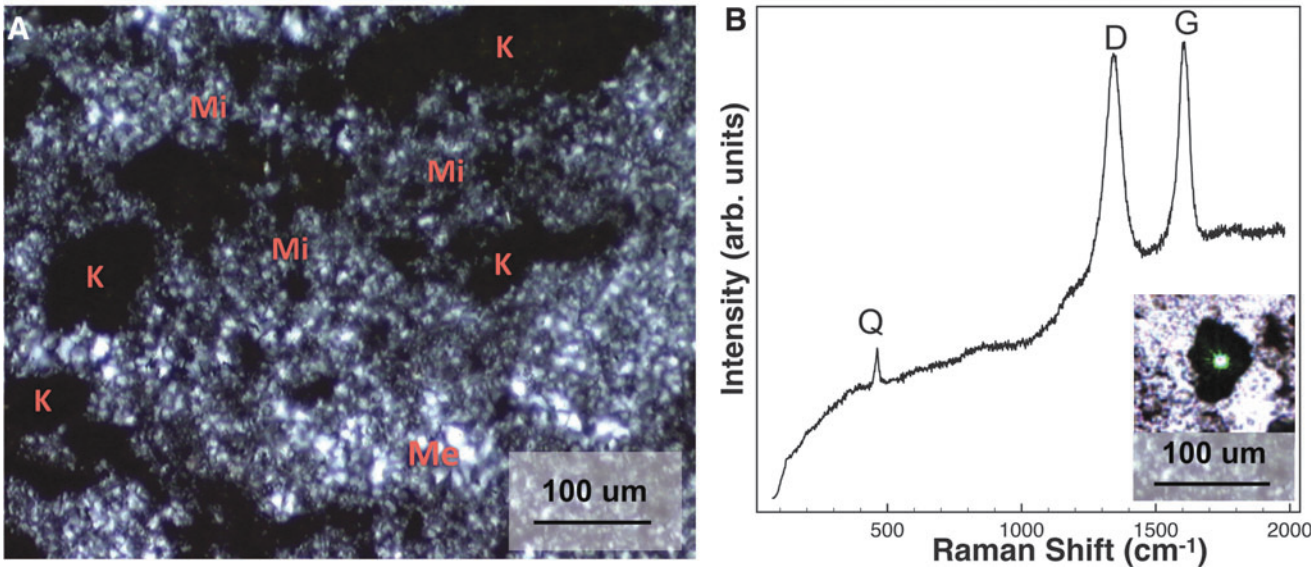

FIG. 2. Characterization of the hydrothermal chert. **(A)** Cross-polarized light photomicrograph of the Strelley Pool chert. Black grains, interpreted to be kerogen (K), are surrounded by gray microcrystalline quartz (Mi). Patchy megaquartz (Me) regions appear lighter. **(B)** A representative CW Raman spectrum was acquired on the candidate kerogen region shown in the inset with the laser spot on the grain interrogated. It shows both the main vibrational band for quartz (''Q''; 464 cm^{-1}) captured in the laser's sampling volume and D and G bands (1345 and 1602 cm^{-1}) with low background fluorescence relative to the high Raman signal intensity.

grains. Pyrite was usually associated with kerogen (Fig. 4C, D) and occurred as framboids, which in some cases is biomediated (Popa *et al*., 2004). Well-preserved fossils are known in this formation (Muller *et al*., 2009), consistent with our observations. Kerogen and the matrix both displayed moderately high fluorescence under visible CW Raman spectroscopy, necessitating high laser powers for spectral features to be seen with this technique (Fig. 4D). This is because high laser powers (in this sample, 12 mW, increased from previous attempts at 6 mW and below) prolonged exposure and burned away (photoquenched) the source of the fluorescence (Bozlee *et al*., 2005). This allowed Raman detection.

3.4. Permian sulfate evaporite, Castile Formation, Delaware Basin, Texas

Castile Formation deep-water evaporites were deposited in the Delaware Basin during the late Permian. Deposits consist of light-toned layers of primary anhydrite ($CaSO_4$), alternating with dark-toned primary carbonates that nucleated in the water column, and settled to the bottom of the basin to form laminated (varved) sulfate–carbonate deposits (Anderson *et al*., 1972). Exposure to groundwater caused anhydrite to form gypsum and resulted in compressional folding of laminae (Scholle *et al*., 1992). Dark laminae are composed of fine-grained, organic-rich carbonate mud (micrite), containing both dolomite and calcite (Fig. 5 and Table 1). Lighter laminae are dominated by coarser euhedral sulfate (gypsum and anhydrite) crystals (Fig. 5; Table 1).

Microscopy analyses revealed that dark particulate grains, consistent with kerogen, occurred abundantly in dark carbonate-rich laminae (Figs. 5C and 10B), consistent with previous descriptions of organic-rich carbonate laminations in the Castile Formation (Anderson *et al*., 1972). Kerogen and matrix minerals were detected with visible CW Raman spectra, despite generally high background fluorescence (Fig. 5C), often requiring high powers (up to 6 mW) to induce photoquenching (Bozlee *et al*., 2005).

3.5. Holocene stromatolitic limestone (carbonate), Walker Lake, Nevada

The sample analyzed was collected from a high stand terrace along the western shoreline of Walker Lake (Osborne *et al*., 1982). It consists of alternating dark (kerogen-rich) and light laminae (mostly calcite; Table 1), as seen under microscopy (Figs. 6A and 10G) and confirmed by Raman analyses (Fig. 6B).

Dark laminae contained abundant opaque candidate kerogen grains as both irregular patchy aggregates and morphologically distinct filaments (Fig. 6B), consistent with previous descriptions of filamentous algae commonly observed in carbonate-rich layers of this sample (Osborne *et al*., 1982). Detrital grains of quartz and plagioclase feldspar were also present (Table 1). Kerogen and calcite both appeared highly fluorescent in visible CW Raman spectra. With a low laser power setting (1.3 mW), fluorescence often swamped the Raman signal (Fig. 6B spectrum 1). Laser powers were increased from 1 to 6, 12, and finally 28 mW, which photoquenched the fluorescence (Bozlee *et al*., 2005) and produced the clearest spectra with calcite and D and G bands (Fig. 6B).

To more fully understand the nature, size, and distribution of kerogen and other organics in this sample (detailed in Section 4.1), we performed confocal Raman imaging spectroscopy (CRIS) on a sample chip of the stromatolitic limestone (Fig. 6C–G). We identified two categories of organics dispersed throughout the matrix, including abundant kerogen present at spatial scales of $\sim$10 microns to submicrons. Second, less mature organics were indicated by CH_2 and CH_3 stretch bands at similar scales. The latter bands correspond to many possible

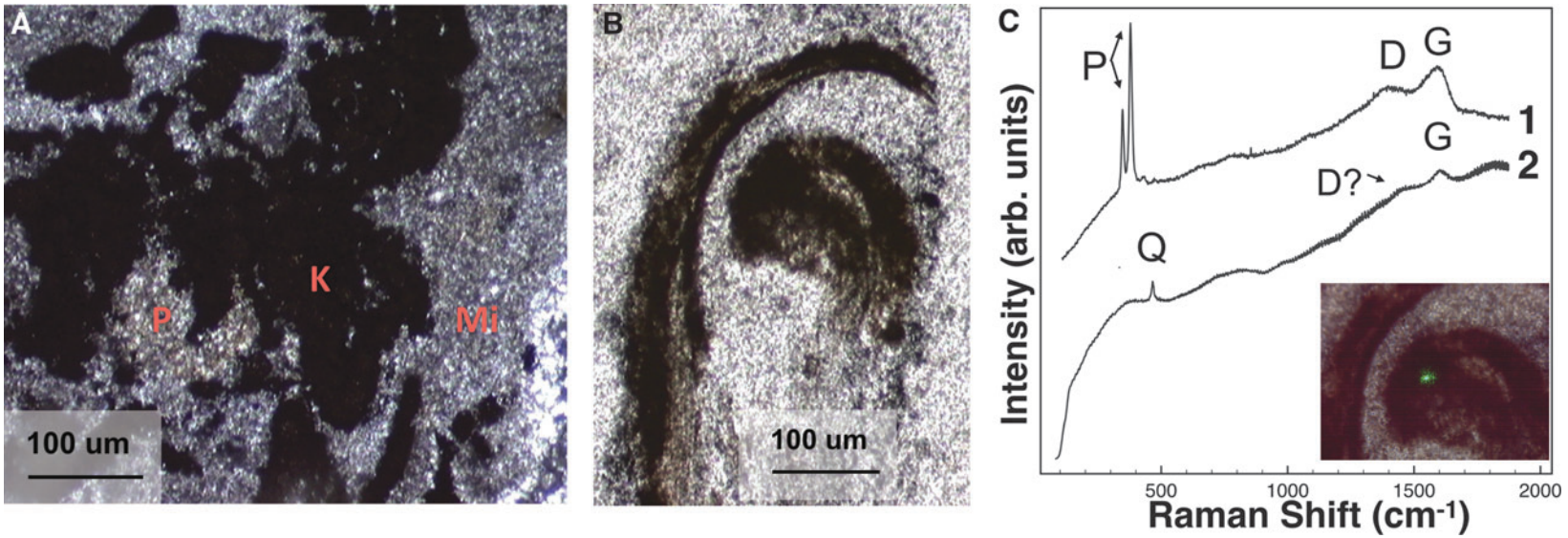

FIG. 3. Characterization of the silicified shale. **(A)** Cross-polarized light photomicrograph showing a region of what is interpreted to be kerogen (K) and brassy pyrite (P), surrounded by microcrystalline quartz (Mi). **(B)** Plane-polarized light photomicrograph showing morphologically distinct kerogen. **(C)** Spectrum 1 is a representative CW Raman spectrum showing the association of D and G bands (1590 and 1390 cm^{-1}) with pyrite (''P''; 346 and 378 cm^{-1}). Spectrum 2, acquired on the feature in **(B),** shown with the green CW laser in the inset, reveals a quartz matrix band (465 cm^{-1}), a G band at 1590 cm^{-1}, and a possible D band, obscured by high fluorescence.

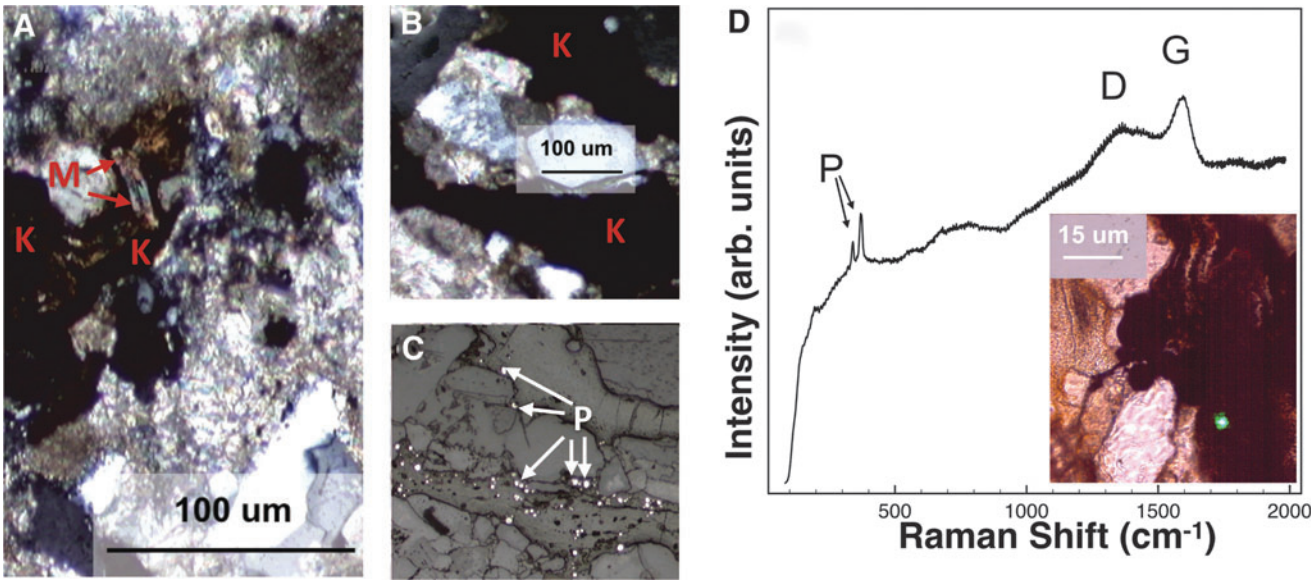

FIG. 4. Characterization of the marine sandstone. **(A)** Cross-polarized photomicrograph showing kerogen (K) associated with platy mica (M), either muscovite or phlogopite, based on Raman analysis (Table 1), surrounded by a dolomite/calcite cement (light regions). **(B, C)** Plane-polarized light and reflected light photomicrographs, respectively, of the same region, showing that pyrite (P) appears shiny and associated with kerogen. **(D)** A representative CW Raman spectrum is shown, acquired with the visible CW Raman spectroscopy at 12 mW power on the spot indicated by the green laser in the inset. It shows D and G bands (1369 and 1589 cm^{-1}) associated with pyrite (346 and 378 cm^{-1}) and a broad unidentified region at $\sim$800 cm^{-1}.

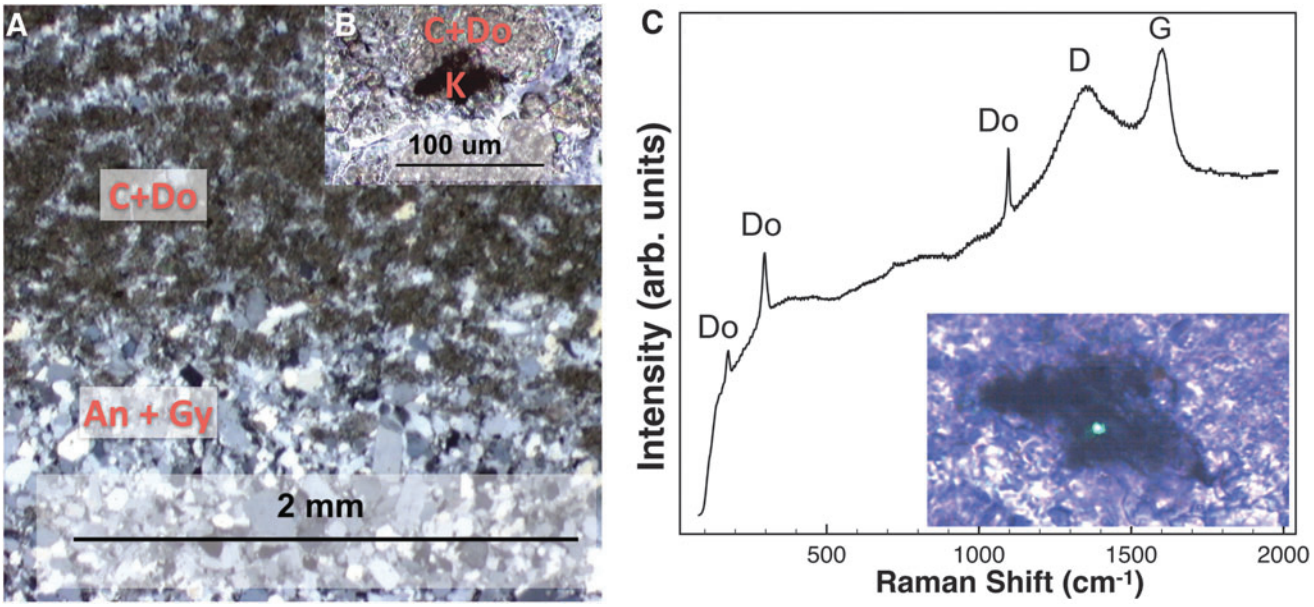

FIG. 5. Characterization of the sulfate evaporite. **(A)** Cross-polarized light photomicrograph showing carbonate (as calcite, C, and dolomite, Do) and sulfate laminae (as anhydrite, An, and gypsum, Gy). Sulfate grains appear black, gray, or white, depending on their extinction in cross-polarized light. **(B)** Cross-polarized light photomicrograph showing a candidate kerogen grain preserved in carbonate, interrogated with visible CW Raman spectroscopy as shown in the inset in **(C)**. **(C)** Visible CW Raman spectrum of suspected kerogen grain in a carbonate lamina. Inset: Laser spot on the region interrogated, on the same grain as in **(B)**. The resulting spectrum revealed D and G bands (1351 and 1601 cm^{-1}) and dolomite (175, 299, and 1095 cm^{-1}).

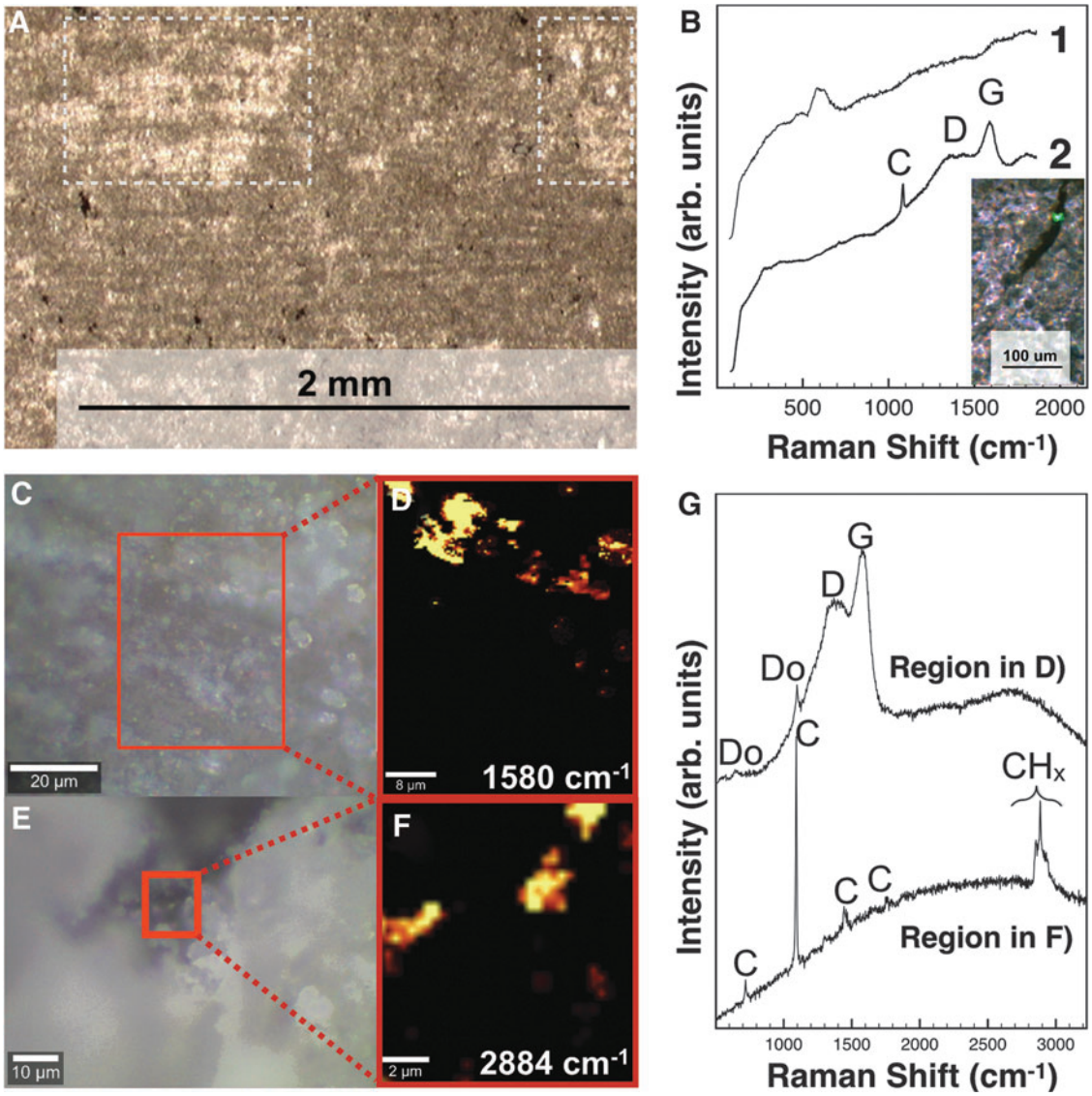

FIG. 6. Characterization of the stromatolitic limestone. **(A)** Plane-polarized light image showing of microcrystalline carbonate-rich (light) and kerogen-rich (dark) laminae with interruptions of lighter patchy carbonate (dashed boxes), interpreted to be due to recrystallization. **(B)** Filamentous kerogen regions, such as the one in the inset shown in plane-polarized light, were interrogated with visible CW Raman spectroscopy. Spectrum 1 was taken at 1.3 mW laser power; spectrum 2 was taken on a similar grain at 28 mW power. Spectrum 1 is dominated by fluorescence (except for an unidentified band at $\sim 600\,cm^{-1}$). Spectrum 2 shows D and G bands (1353 and 1588 cm^{-1}) and calcite (1086 cm^{-1}). **(C, E)** Reflected light photomicrographs of the stromatolite. Boxes: CRIS-analyzed regions in **(C**, **E)**, respectively. **(D, F)** Raman intensity maps of the G band (centered at 1580 cm^{-1}) and the 2884 cm^{-1} band (C-H stretch), respectively. Yellow pixels denote higher relative band intensity. **(G)** Representative single-pixel Raman spectra are shown of the most intense pixels from maps in **(C)** in the top and in **(E)** in the bottom spectra. G and D ($\sim 1380\,cm^{-1}$) bands and CH_x stretch bands (2853, 2884, and $\sim 2930\,cm^{-1}$) are indicated, along with dolomite (Do; 725 and 1097 cm^{-1}) and calcite (C; 711, 1085, 1435, and 1750 cm^{-1}) from the mineral matrix. CRIS, confocal Raman imaging spectroscopy.

organic functional groups that are less thermally altered and physically compacted than kerogen, including microfossil cell wall structures (Socrates, 2004; Marshall *et al*., 2006).

3.6. Eocene lacustrine carbonate, Green River Formation, Wyoming

The Green River Formation consists of several members having different compositions (*e.g.*, Surdam and Stanley, 1979). The sample analyzed here is from a lacustrine limestone member, formed by precipitation of fine-grained (micritic) carbonate. The carbonate unit precipitated as calcite and dolomite within the water column and settled to the lake bottom (Desborough, 1978).

We observed both microscopic particulate kerogen (Fig. 7A) and macroscopic well-preserved fossils (not analyzed here). Kerogen is dispersed throughout a carbonate-rich matrix, mainly as calcite and dolomite (Table 1). This description is consistent with previous descriptions of abundant and diverse organics (kerogen, coals, more immature algal and mollusk

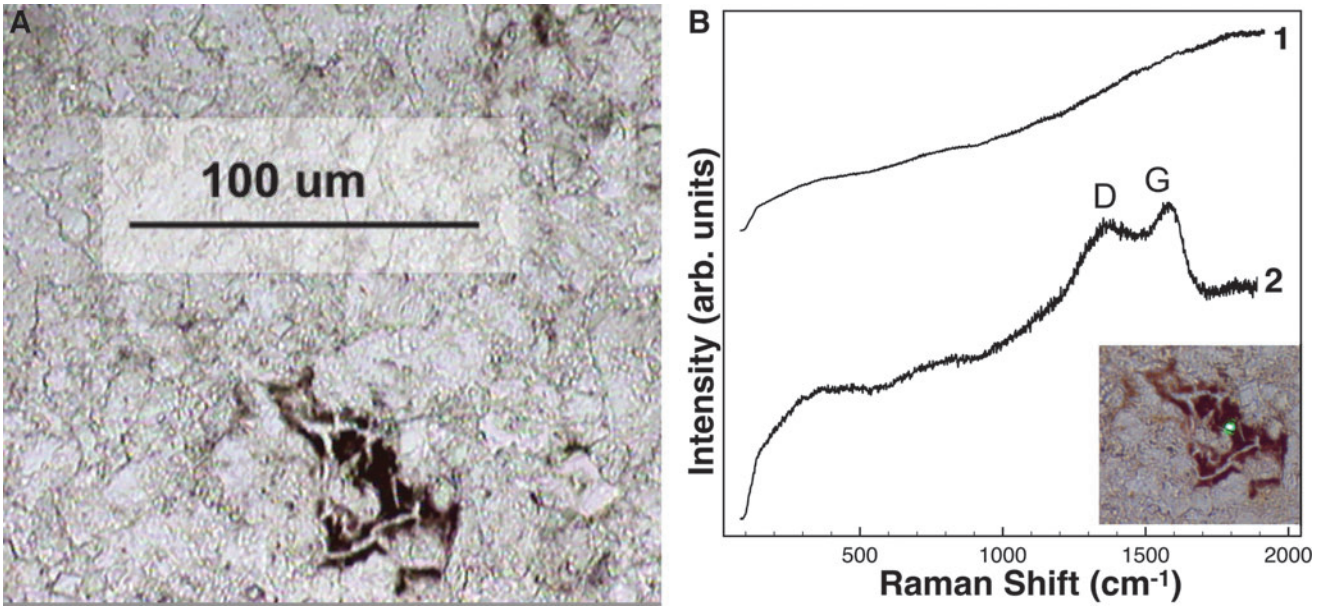

FIG. 7. Characterization of the lacustrine carbonate. **(A)** Plane-polarized light image showing a fine-grained carbonate surrounding a dark candidate kerogen region. **(B)** Visible CW Raman spectra of carbonate (spectrum 1) surrounding the candidate kerogen grain (spectrum 2) shown in **(A)** are presented. The inset shows the laser on the grain interrogated. Spectrum 1 shows only high fluorescence; spectrum 2 reveals D and G (1351 and 1583 cm^{-1}) bands.

remains, etc.) found in carbonate-rich members of this formation (Surdam and Stanley, 1979). In visible CW Raman spectra, high fluorescence prevented the detection of the carbonate matrix (Fig. 7B spectrum 1) but not kerogen preserved within it (Fig. 7B spectrum 2).

3.7. Miocene–Pliocene evaporitic mudstone, Verde Basin, AZ

This clay-rich playa evaporite was deposited within the Verde Basin during the Miocene–Pliocene. The evaporitic playa mudstone sequence was followed by the formation of a perennial lake during the Pliocene with the deposition of basin-wide lacustrine carbonate sediments (Bressler and Butler, 1978; Nations *et al*., 1981). The mudstone is cemented primarily by carbonate (as magnesite) and fine-grained clays, especially smectites (Fe- or Mg-rich saponite and montmorillonite), as confirmed with XRPD (Table 1).

Microscopy revealed other phyllosilicates, present as detrital grains, along with a variety of other abundant coarse angular grains and evaporite phases present (Fig. 8A, B and Table 1). Thin section microscopy revealed the presence of clasts with rust-colored alteration rims, suspected to be iron-rich phases, and dark grains in moderate abundance scattered throughout the matrix (Fig. 8C), interpreted as kerogen candidates. Other phases with optical properties consistent with iron oxides were also seen abundantly with microscopy and identified as hematite with CW Raman analyses (Fig. 8D spectrum 2) and as goethite and lepidocrocite as identified with other techniques (Table 1). XRPD did not identify any iron phases (Table 1).

Fossils have been noted in Verde Formation but not in the sequences we sampled (Wadell, 1972). In our analyses, all CW visible Raman spectra of candidate kerogen grains and the mudstone matrix were overwhelmed by fluorescence, regardless of the acquisition setting (Fig. 8D).

3.8. UV-TG Raman results

UV-TG Raman spectra of kerogen and matrix areas in samples are shown in Fig. 9, along with kerogen and mineral standards for comparison. In the chert sample, UV-TG Raman spectroscopy of candidate kerogen regions revealed quartz (at 465 cm^{-1} and less intense bands at 809, 1084, and 1171 cm^{-1}) along with an intense G band (1586 cm^{-1}), plus a convolution of two second-order bands spanning $\sim$2900 to $\sim$3300 cm^{-1} and centered at $\sim$3100 cm^{-1} (Fig. 9A spectrum 1).

The lack of the D band in UV Raman spectroscopy is attributed to the sample's high thermal maturation, which caused highly graphitic (Ferrari and Robertson, 2001) and thermally mature (Bower *et al*., 2013) carbon in that sample, which can be seen as the intense G band (see Section 1.2 for details).

The organic bands of the chert's spectrum are comparable with those of the kerogen standard (Fig. 9A spectrum 2), including the second-order region at $\sim$2900 to $\sim$3300 cm^{-1} (Fig. 9A inset). Similarly, when candidate kerogen regions were interrogated in the silicified shale, the main quartz matrix band was identified, along with a G band (ranging from 1600 to 1609 cm^{-1} in spectra of this sample) and a broad D band spanning from $\sim$1200 to 1500 cm^{-1} (Fig. 9A spectrum 3). Short- and long-gated UV Raman interrogations of the same sample's matrix (Fig. 9B spectra 13–14) both revealed similar spectra: a G band and the main quartz band.

The marine sandstone revealed both G bands (spanning from 1586 to 1611 cm^{-1}, respectively) and weaker D bands (centered at $\sim$1370 cm^{-1}) in two different candidate kerogen regions. One region (pictured in Fig. 10D) captured dolomite (at 1098 cm^{-1}) in the sampling volume (Fig. 9A spectrum 5), and the other revealed both D and G bands in both long- and short-gated spectra (Fig. 9B spectra 15–16). Fluorescence (especially >2000 cm^{-1}) was higher in the region containing organics with dolomite captured in the sampling volume (Fig. 9A

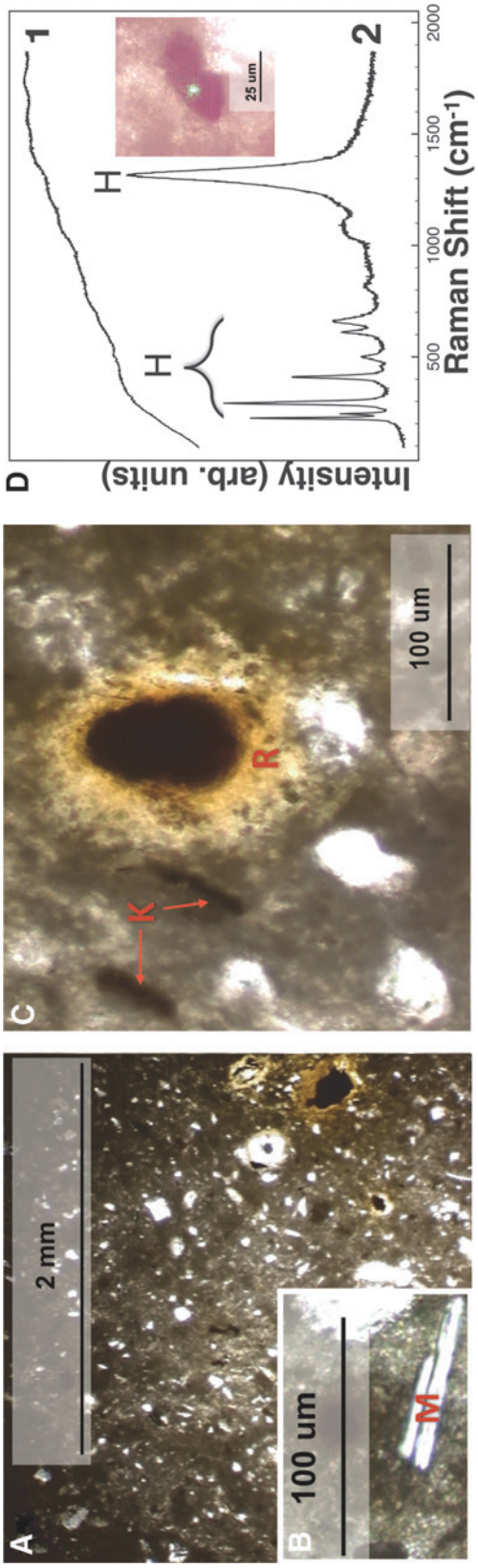

FIG. 8. Characterization of the evaporitic mudstone. Plane-polarized light photomicrographs of the fine-grained matrix, showing **(A)** abundant detrital grains, **(B)** a coarse-grained platy mica, and **(C)** a dark clast with a hazy orange rim, R, and two suspected kerogen grains also indicated. **(D)** Spectrum 1: visible CW Raman spectrum representative of all candidate kerogen grains interrogated, such as that shown in the inset, revealing only prohibitive wavy fluorescence. Spectrum 2: Hematite ("H"; 222, 245, 292, 409, 501, 611, 668, 1070, and 1317 cm^{-1}), obtained on a large opaque grain similar to that shown in (**C**).

spectrum 5) than in the region containing kerogen features alone (Fig. 9B spectra 15 and 16).

In the stromatolite sample (Fig. 9A spectrum 7), UV-TG Raman spectroscopy revealed calcite (1086, 1430, and 1750 cm^{-1}) and a G band ($\sim$1606 cm^{-1}), with moderate fluorescence visible past 2000 cm^{-1} in a candidate kerogen region. A tentative D band seemed to be masked by an overlapping 1430 cm^{-1} calcite band.

In contrast, in the lacustrine carbonate sample (Fig. 9A spectrum 8), the D band, although likely convolved with a sharp calcite band ("C+D"), was more clearly visible, along with second-order features in a targeted candidate kerogen grain. The G band was centered at 1594–1608 cm^{-1} in UV-TG Raman spectra of the lacustrine carbonate. Comparing long- and short-gated spectra of the lacustrine carbonate matrix (Fig. 9B spectra 11–12), fluorescence past 2000 cm^{-1} was slightly reduced with short gating and revealed a weak sharp calcite band at 1430 cm^{-1} and second-order kerogen bands at 2920 and 3250 cm^{-1} that were not seen with long gating.

In the sulfate evaporite sample (Fig. 9C), calcite (1086 cm^{-1}) and/or gypsum (412, 493, 612, 672, 1008, and 1140 cm^{-1}) could be identified when regions without kerogen within both laminae were interrogated (Figs. 10G and 9C spectra 17–21). With long gating (Fig. 9C spectrum 17), it was ambiguous whether the calcite band was present at 1750 cm^{-1}, but with short gating, calcite was seen clearly (Fig. 9C spectrum 18). The G band was present in all cases (at 1590 cm^{-1}), and the D and G bands appeared when a candidate kerogen grain (the same one pictured in Fig. 10E) was interrogated with UV-TG Raman spectroscopy (Fig. 9C spectrum 21).

The evaporitic mudstone was the only sample in which UV-TG Raman analyses did not yield any compositional information (Fig. 9A spectrum 10) when both matrix regions (shown in Fig. 10H) and suspected kerogen regions were targeted for analysis.

3.9. UV-TG fluorescence results

Short- and long-gated fluorescence spectra of kerogen and matrix areas, as well as kerogen and mineral standards, are shown in Fig. 10A–C. These spectra can be broadly grouped into two categories: Types 1 and 2.

Type 1 spectra (Fig. 10A, spectra 1–4), as well as the kerogen standard (spectrum 5), show a very broad feature (likely a convolution of multiple features) centered around $\sim$430 nm, spanning from $\sim$300 to >500 nm. These spectra were acquired on kerogen grains targeted with microscopy (Fig. 10D–F).

Type 2 fluorescence spectra (Fig. 10B, spectra 6–10) show a convolution of two or more bands between $\sim$400 and $\sim$500 nm, with peaks at $\sim$415 nm and slightly less intensely at $\sim$430 nm. These spectra were acquired in regions where kerogen was not targeted for analysis and not visible on the sample surface with microscopy. These spectra are distinctly different from Type 1 spectra (Fig. 10A). (Spectrum 1 in Fig. 10A is an exception; it was acquired on a matrix region of a highly kerogenous sample and is addressed in Section 4.1.) A spectrum acquired on a sticker marker (Fig. 10B, spectrum 11) displays features similar to Type 2 spectra with the addition of a feature at $\sim$515 nm.

We also acquired fluorescence spectra of mineral standards (Fig. 10C) reflecting the major matrix minerals in our

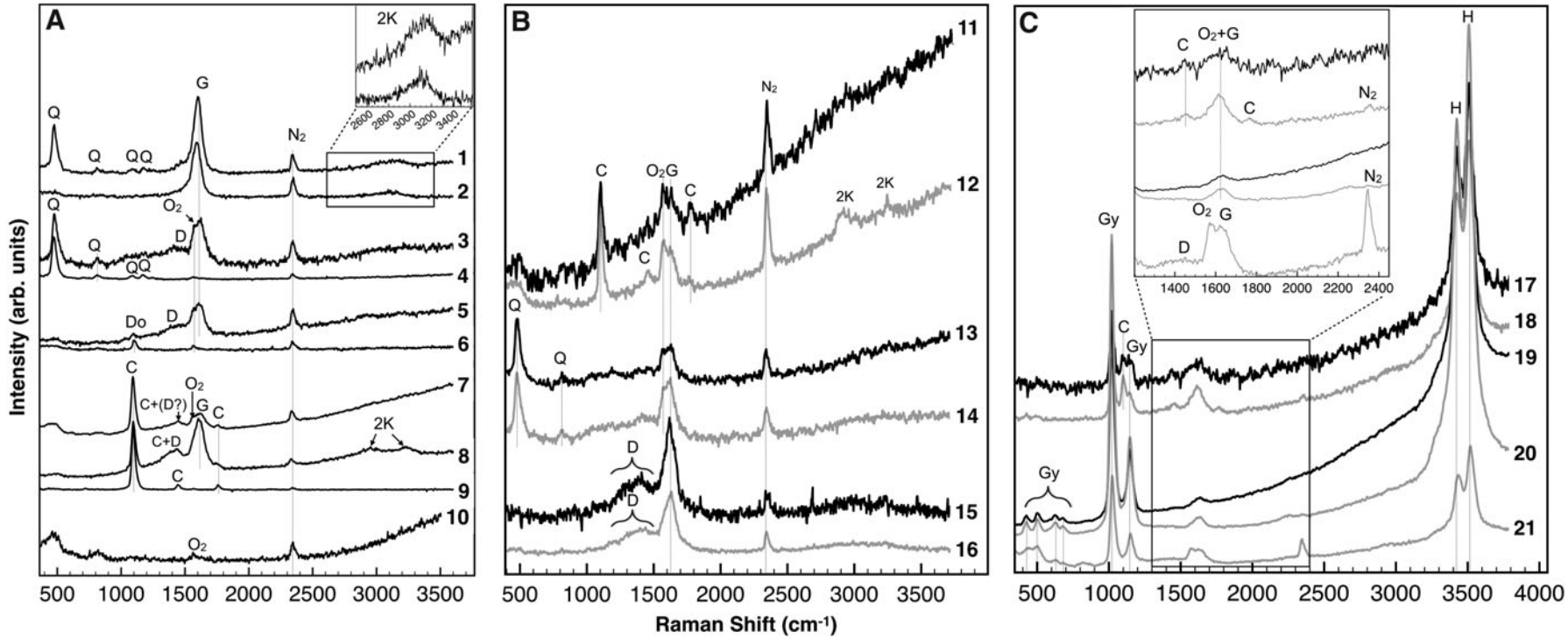

FIG. 9. Representative UV-TG Raman spectra of samples and standards. **(A)** Short-gated Raman spectra of (1) targeted kerogen grain in chert, (2) kerogen standard, (3) targeted kerogen grain in silicified shale, (4) silica sand standard, (5) targeted kerogen grain in marine sandstone, (6) dolomite standard, (7) targeted kerogen grain in light lamina of stromatolitic limestone, (8) targeted kerogen grain in lacustrine carbonate, (9) calcite standard, (10) evaporitic mudstone, representative of both targeted kerogen and mineral matrix regions. Inset: magnified 2K bands in the chert and kerogen standard. Quartz objective interference appears as a broad band $<500\,cm^{-1}$ (spectra 7 and 10). **(B)** Spectral pairs acquired on the same region in long (black) and short (gray) gated modes. Spectra 11–12: lacustrine carbonate, matrix region; spectra 13–14: silicified shale, matrix region; spectra 15–16: marine sandstone, candidate kerogen grain. **(C)** Sulfate evaporite spectra, shown separately for clarity due to different intensity scales. Long (black) and short (gray) gated spectra acquired on the same region of a carbonate lamina (spectra 17–18) and a sulfate lamina (spectra 19–20). Spectrum 21 is a short-gated acquisition of a candidate kerogen grain. Spectra in **(C)** show gypsum bands (''Gy''; 1009 and 1135 cm^{-1}) and H_2O stretch modes (''H''; $\sim$3400 and $\sim$3500 cm^{-1}), common in hydrated sulfates (Wang *et al.*, 2006). N_2 indicates atmospheric nitrogen at 2331 cm^{-1}; O_2 indicates atmospheric oxygen at 1556 cm^{-1} (Hug *et al.*, 2005), appearing in some spectra as convolved with the G band. Other symbols are as in previous figures. All spectra are normalized to the strongest peak and offset for comparison.

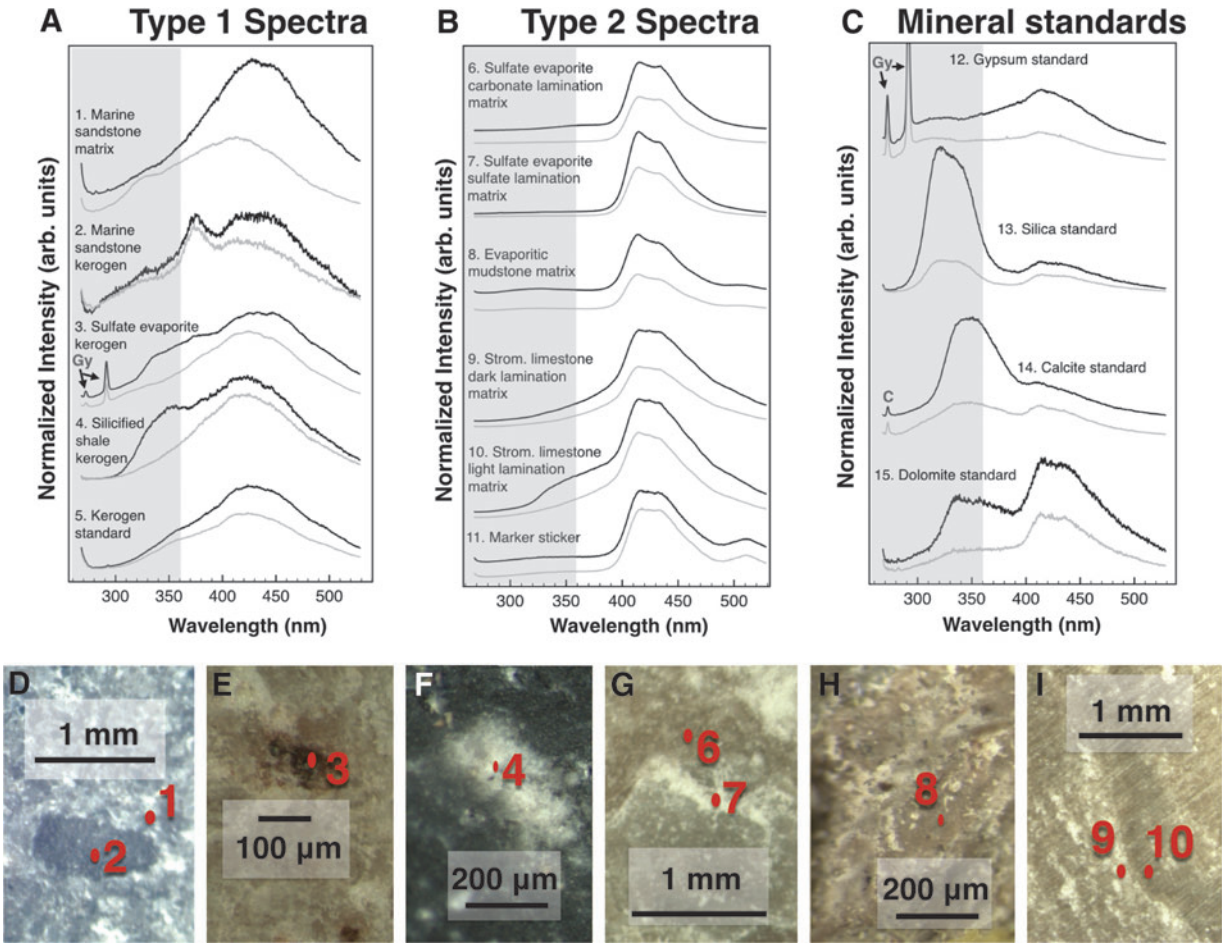

FIG. 10. Representative UV-TG fluorescence spectra of samples and standards. **(A–C)** Shown are long-gated (black) and short-gated (gray) pairs of spectra acquired on the numbered regions denoted in the images of **(D–I)**. Spectra are grouped into **(A)** Type 1, acquired on kerogen grains; **(B)** Type 2, acquired on matrix regions where kerogen was not visible on the sample surface; and **(C)** mineral standards. Sharp bands <300 nm are Raman bands from calcite **(C)** or gypsum (Gy). Gray shaded regions in all panels indicate SHERLOC's fluorescence range (Beegle *et al.*, 2014). All spectra are normalized to the strongest peak and offset for comparison. **(D–I)** Reflected light photomicrographs of sample chips show where spectra in **(A, B)** were taken. Red spots show the approximate laser spot position on **(D–F)** candidate kerogen and **(G–I)** mineral matrix regions targeted for colocated UV-TG Raman and fluorescence analyses. Numbered spots correspond to labeled spectra.

samples. These spectra also display features at 415–430 nm, similar to Type 2 spectra, along with intense features <400 nm.

Other fluorescence features are visible with peaks at or <375 nm in both Types 1 and 2 spectra. Features at these wavelengths can have organic or inorganic sources with UV excitation (Abbey *et al.*, 2017 and references therein). In this study, we only focus on features peaking between 400 and 450.

To quantify the effect of gating on fluorescence reduction with UV-TG Raman spectroscopy, time-resolved fluorescence spectra were obtained on the silicified and marine sandstones, both lamina types in the sulfate evaporite, the lacustrine carbonate, and three mineralogically diverse matrix regions of the stromatolitic limestone.

Our quantification method is illustrated in Fig. 11. For each sample, fluorescence spectra were obtained by using intensity I, time t, and wavelength λ parameters detailed in Section 2.5. For each sample, we selected a wavelength at which the spectral intensity had a local maximum at I_{max} >400 nm (Fig. 11A) and I_{max} <400 nm (Fig. 11D). The specific wavelength, identified by an asterisk in Fig. 11A and E, varied slightly across samples. At this wavelength, the (I, t, λ) data were ''sliced'' in the time domain to obtain the associated fluorescence decay curves $I(t)$ (Fig. 11B, F). Next, we summed each decay curve to obtain the cumulative fluorescence signal, F_{tot}, and overlaid it on the cumulative Raman signal of a gypsum standard at the wavelength corresponding to the strongest Raman band, 1008 cm^{-1}, or R_{tot} (Fig. 11C, G). We assume that Raman scattering is effectively instantaneous on the fluorescence time scales measured here, and, therefore, that any Raman signal of any sample would have the same temporal profile. This allowed the quantification of gating efficiency as R_{tot}/F_{tot} (Fig. 11D, H).

4. Discussion

4.1. Kerogen detection with combined UV-TG Raman and fluorescence data sets

Goal 1 of our study was to explore the capabilities of UV-TG Raman and fluorescence spectroscopies for detecting naturally preserved kerogen in our complex, natural samples as a potential biosignature. Our UV-TG Raman spectra reveal that vibrational bands diagnostic of various aromatic

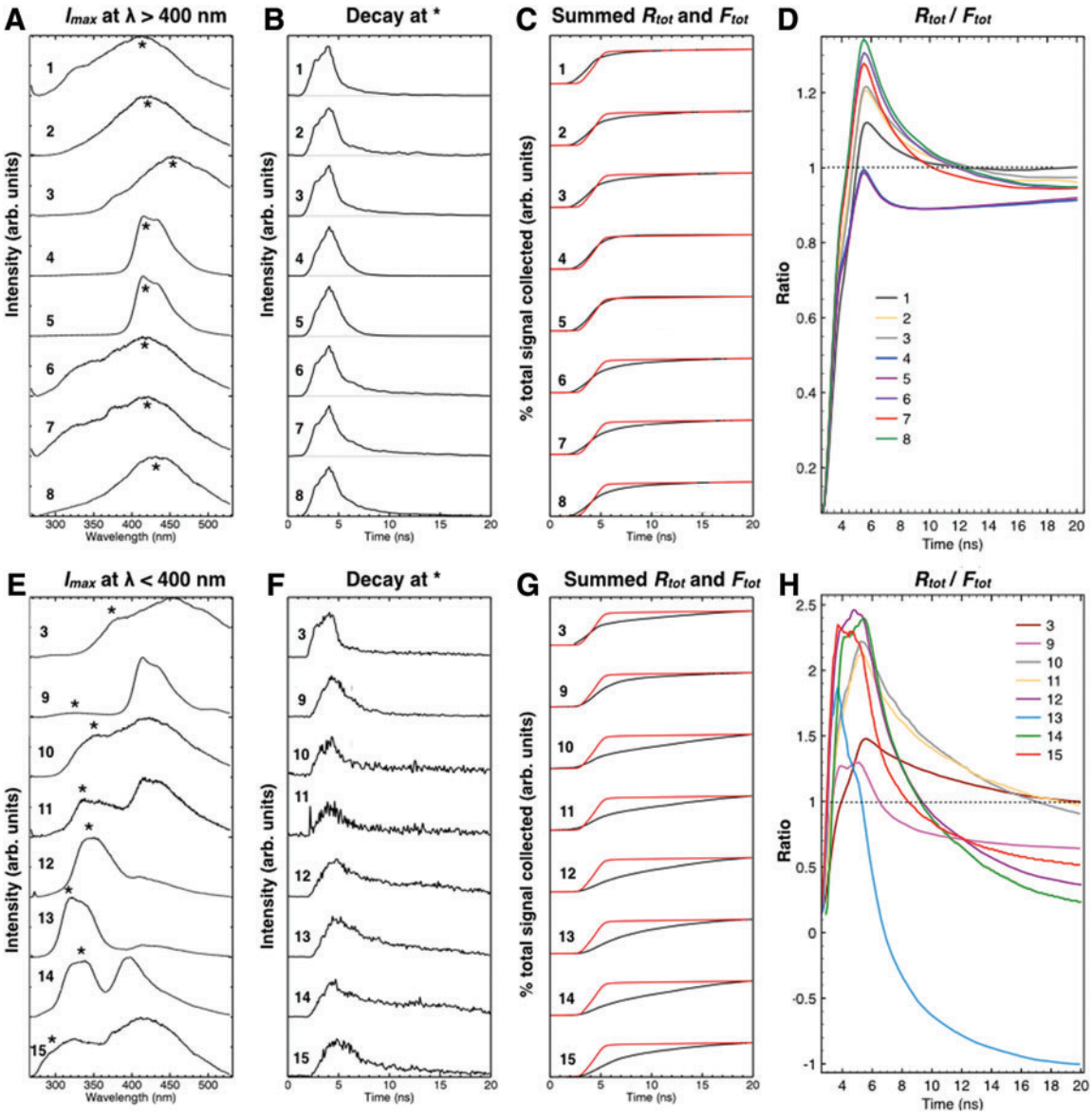

FIG. 11. Quantification of gating effects on fluorescence reduction. **(A, E)** Short-gated fluorescence spectra on which wavelengths with **(A)** I_{max} >400 nm and **(E)** I_{max} <400 are indicated by an asterisk. Spectra are numbered as follows: (1) Marine sandstone matrix first region; (2) siliceous sandstone, kerogen; (3) lacustrine carbonate, kerogen; (4) sulfate evaporite, carbonate lamina; (5) sulfate evaporite, sulfate lamina; (6) stromatolitic limestone, matrix second region; (7) stromatolitic limestone, matrix region 2; (8) stromatolitic limestone, matrix third region; (9) evaporitic mudstone, matrix; (10) silicified shale matrix; (11) dolomite standard; (12) calcite standard; (13) silica sand standard; (14) stromatolitic limestone matrix fourth region; and (15) stromatolitic limestone fifth matrix region. Decays of the fluorescence intensity at λ(I_{max}) through the 20-ns spectral acquisitions in **(A, E)** are shown in **(B, F)**, respectively. In **(B, F)**, the *y* axis represents the intensity of a signal accumulated between the gate delay plus 3 ns. Integrals of fluorescence decays, or F_{tot}, are shown in **(C, G)** over the 20-ns acquisition (black); overlaid is an integrated Raman spectrum of the gypsum standard, R_{tot}, acquired with the same settings as the fluorescence data (red). In panels **(D, H)** are shown ratios of R_{tot}/F_{tot} as a function of time for **(D)** I_{max} >400 nm and **(H)** I_{max} <400 nm. The dotted line indicates $R_{tot} = F_{tot}$. (Color graphics are available at www .liebertonline.com/ast)

carbonaceous compounds, including kerogen, are visible for all samples except the evaporitic mudstone (Section 4.3).

UV-TG Raman spectra usually reveal both the D and G bands (whose peak centers varied across samples) present (*e.g.*, Fig. 9 spectra 5, 15, 16, and 21), or only the G band present (*e.g.*, Fig. 9 spectrum 1). The significance of G band peak variation and what it may reveal about carbon structure, maturity, and bonding have been discussed elsewhere (Ferrari and Robertson, 2001; Ferrari and Robertson, 2004; Allwood *et al.,* 2006; Bower *et al.,* 2013 and references therein). Additional weaker bands at 2900–3300 cm^{-1} are present in some spectra (*e.g.*, Fig. 9 spectra 1, 8, and 12), commonly attributed to second-order bands of highly graphitic carbon or kerogen (Section 1.2). In other instances, the G band is present with a weak, ambiguous D band, sometimes masked by a weak 1430 cm^{-1} calcite band in calcite-rich samples (Fig. 9 spectra 7–8).

D and/or G bands (and second-order bands) were always detected on grains suspected to be kerogen based on prior microscopy, whereas when mineral standards were interrogated, these vibrational bands were always absent (*e.g.*, Fig. 9 spectra 4, 6, 9). But why was a G band usually present when mineral matrices were interrogated? UV-TG Raman spectra did not enable us to distinguish C=C aromatic components in kerogen, other types of organics (*e.g.*, trace intracrystalline organics in the matrix), even if they are also potential biosignatures, or similarly structured abiogenic contaminants (deposited on the sample surface).

Our confidence in identifying UV-TG Raman bands caused by kerogen was strengthened only after examining colocated UV-TG fluorescence data acquired on candidate regions preselected by microscopy. UV-TG fluorescence results reveal two broad types of fluorescence features in all samples (Fig. 10A, B), although there are additional variations across each type. Both types of fluorescence are interpreted to be organic because they are present in both long- and short-gated spectra, suggesting that their decay lifetimes are short and consistent with organic sources (Section 1.4).

We interpret Type 1 fluorescence features, combined with D, G, and/or second-order UV-TG Raman bands on colocated microscale regions, as being due to organics contained in kerogen, such as hydrogenated amorphous carbon compounds, primarily PAHs, for the following reasons.

First, Type 1 fluorescence spectral features were obtained on spots in which candidate kerogen regions were previously targeted with microscopy analyses (Fig. 10D–F).

Second, the ~300–500 nm feature in Type 1 spectra has a comparable morphology with the kerogen standard (Fig. 10A spectrum 5), likely because kerogen contains a complex mixture of many PAHs, which commonly have fluorescence features peaking in the ~300–500 nm range at $\lambda_{ex} = 266$ nm (Apicella *et al.*, 2004).

Third, these UV-TG Raman spectra are similar to spectra containing both D and G bands of kerogen-containing fossil ferns (Czaja *et al.*, 2009), and to spectra of amorphous and hydrogenated amorphous carbon, which is compositionally similar to kerogen (Ferrari and Robertson, 2004), both at UV excitation ($\lambda_{ex} = 244$ nm).

Type 1 spectra correspond to sample spots whose UV-TG Raman spectra contain both D and G bands. The chert is an exception, lacking the D band, but the presence of both a G band and second-order Raman bands is consistent with highly graphitic, thermally mature kerogen, common in that sample, and closely matches the Raman spectrum of the kerogen standard (compare Fig. 9 spectra 1 and 2). Another exception is one region in the marine sandstone matrix (Fig. 10A spectrum 1), where a kerogen spot not visible with microscopy was likely captured in the laser sampling volume.

Conversely, spots that revealed Type 2 spectra were usually associated with a weak G band in UV-TG Raman spectra and lacked a D band or second-order bands (Fig. 9 spectra 11–12, 17–20). The D band may have been present but undetectable in these cases since the G band was weak. We interpret Type 2 spectra and colocated UV-TG Raman spectra containing only G bands as caused by organics unassociated with our targeted biosignature (preserved kerogen) for two reasons. First, Type 2 fluorescence spectra (Fig. 10B) were obtained solely on matrix regions where kerogen was not visible with microscopy (Fig. 10G–I). Second, these spectra show a convolution of fluorescence features that significantly differ from those of the kerogen standard (Fig. 10A spectrum 5).

What is the origin of the organics revealing both Type 2 fluorescence and G bands in colocated UV-TG Raman spectra? We hypothesize that various micron-sized, thermally immature organic compounds were present in the mineral matrix of such samples and were undetectable at the resolution of our petrographic microscope or UV-TG Raman and fluorescence imaging systems (and unlikely to be detectable by a rover imager on Mars).

One possible source for these organics may be fulvic acids, a class of compounds often associated with carbonate nucleation (Van Beynen *et al.*, 2001; Neuweiler *et al.*, 2003). Fulvic acids can be the dominant organic fluorophore causing carbonate fluorescence and can produce spectral features that are similar to Type 2 features (Sierra *et al.*, 1994; Neuweiler *et al.*, 2003). It is notable that Type 2 features were visible mainly in carbonate-rich samples. This interpretation is also consistent with the fact that carbonate mineral standards (naturally derived dolomite and calcite; Fig. 10C) also contained weak Type 2 features.

In one carbonate sample displaying Type 2 fluorescence features, we performed CRIS to elucidate the nature, size, and distribution of organics it preserved. Two categories of micron to submicron-sized organics dispersed throughout the matrix were identified (Fig. 6C–G): (1) kerogen and (2) less mature organics corresponding to many possible organic functional groups, including microfossil cell wall structures (Socrates, 2004; Marshall *et al.*, 2006). By extension, such organics can also exist in other samples.

Neither category is likely to be a surface contaminant, since the sample was abraded (Section 2.5) and since organics were seen uniformly distributed throughout the sample. Neither type of micron-scale feature would be resolvable with the petrographic microscope or the UV-TG system. These organics may be composed of a variety of organic species trapped into an intracrystalline organic fraction during mineral precipitation (*e.g.*, Neuweiler *et al.*, 2003). The ambiguous origin of Type 2 features further highlights that natural geological samples preserve complex biosignatures that are not as easy to identify as pure organics.

Our interpretations are consistent with previous reports of organics preserved in our samples. For instance, in Alum Formation marine sandstone, researchers have documented well-preserved fossils thought to originate from fossil arthropods (Muller *et al.*, 2009), consistent with our observations of abundant and quite large kerogen grains (Fig. 10D) and kerogenous Type 1 spectra in this sample (Fig. 10A spectra 1–2). Verde Formation evaporites are generally fossil poor (Wadell, 1972), consistent with our observation of nonkerogenous Type 2 fluorescence in that sample (Fig. 10B spectrum 8). In the Castile Formation sulfate evaporite, the presence of kerogenous and nonkerogenous organics mainly in the carbonate laminae (Figs. 9C and 10B, spectrum 6, and Fig. 10A, spectrum 3) is consistent with the literature (Anderson *et al.*, 1972), which suggests that this is due to phytoplankton production during the carbonate deposition season. This is also true in the Walker Lake stromatolitic limestone's carbonate laminae (Osborne *et al.*, 1982) and consistent with our observations of kerogenous and nonkerogenous organics in that sample's carbonate laminae (Type 2 organics, Fig. 10B spectra 9–10; Fig. 6).

One could argue that thermally immature or disordered organics trapped in the mineral matrix underwent ''kerogenization'' under the UV laser beam to yield the graphitic, ordered G bands we detected. However, laser-induced alteration was unlikely with the laser energies we used in our UV-TG Raman analyses: it was not observed in our samples under microscopy postanalysis or in organic analyses when using previous prototypes of this instrument (Eshelman *et al*., 2014; Skulinova *et al*., 2014). One could also argue that Type 2 features were caused by organic-rich surface contaminants. We also deem this unlikely because most sample surfaces were abraded immediately before analysis (Section 2.5).

This work highlights the need for further studies to systematically characterize organics expected on Mars to inform UV Raman and fluorescence biosignature analyses. This includes contaminants (rocket fuel, cosmogenic organics, etc.) and diverse biosignatures beyond kerogen, in natural geological samples and at multiple scales. Our results also highlight the sensitivity of UV λ_{ex} for detecting kerogen as well as other (*e.g*., intracrystalline) organics (*i.e*., Type 1 vs. Type 2 fluorescence spectra) preserved in natural geological samples, either of which may be potential biosignatures.

Additional evidence for the organic origin of Type 1 and 2 fluorescence features could come from fluorescence decay lifetimes of $\lesssim$100 ns (Sharma *et al*., 2003; Bozlee *et al*., 2005). Fluorescence decay lifetimes can be derived from our time-resolved fluorescence data (Fig. 11B, F and Supplementary Fig. S5).

We attempted to calculate decay lifetimes at peak wavelengths of both Type 1 and 2 features using the method of Eshelman *et al*. (2015). However, this method, which assumes that a single component caused the observed fluorescence, produced large uncertainties in our calculated results. This implies that Types 1 and 2 features are caused by multiple mixed components; accurate calculations would require multicomponent analysis that is beyond the scope of this study. This further emphasizes the complex nature of biosignatures in natural samples analyzed with UV spectroscopy methods, in contrast to simple idealized laboratory organics often used as Mars analogues.

4.2. Reducing fluorescence in Raman spectra

In CW Raman spectra, fluorescence often masked matrix mineral and/or kerogen features (*e.g*., Figs. 6B spectrum 1, 7B spectrum 1). In such cases, fluorescence could be reduced only through photoquenching with high laser power, in which case kerogen or matrix features became visible (*e.g*., Figs. 5C, 6B spectrum 2). However, we discourage the use of this method for CW Raman analysis, as it could alter the sample and lead to spurious interpretations (Marshall *et al*., 2010; Jorge-Villar and Edwards, 2013).

With UV-TG Raman spectroscopy, UV λ_{ex} and gating were strategies to reduce fluorescence of kerogen and its host matrix; assessing these strategies was our study's second goal. Our results show that a UV-TG Raman system is suitable to detect the common diagnostic Raman bands associated with naturally preserved kerogen (Section 4.1) and the main vibrational band of its hosting mineral matrix (*e.g*., quartz, dolomite, calcite, and gypsum) in natural samples targeted on Mars; this is achievable without fluorescence interference $<2000\,cm^{-1}$, where diagnostic Raman bands occur.

What were the relative contributions of UV λ_{ex} and gating in reducing fluorescence in Raman spectra? To isolate the effect of λ_{ex} on fluorescence reduction, we acquired long-gated spectra with the UV Raman system to approximate a CW acquisition with UV λ_{ex}. Long gating and $\lambda_{ex} = 266$ nm allowed the identifications of the main matrix mineral (Fig. 9 spectra 11, 13, 17, 19) and kerogen peaks (Fig. 9 spectrum 15). Thus, $\lambda_{ex} = 266$ nm mitigated fluorescence background in our Raman spectra $<2000\,cm^{-1}$. This result builds on previous successful detections of simple synthetic organics using the same UV-TG instrument (Eshelman *et al*., 2014). Additional work should seek to further understand the relationships between other biosignature types expected on Mars and Raman λ_{ex}.

To isolate the effects of gating on fluorescence reduction, we performed two analyses: (1) comparisons of short- and long-gated spectra acquired on the same spots and (2) determination of gate lengths that maximize the Raman signal relative to fluorescence.

Compared with long-gated acquisitions on the same spots, short gating reduced fluorescence $>2000\,cm^{-1}$ (Fig. 9B, C). Short gating was not necessary to identify kerogen first-order bands, but it did enable the identification of an additional weak calcite band and second-order kerogen bands at $>2900\,cm^{-1}$ (Fig. 9; spectrum 12). Second-order bands are complementary but not essential to identify highly graphitic carbonaceous compounds that may or may not be biosignatures (since first-order bands are much more intense), neither in our samples nor on Mars.

To determine optimal gate lengths, we examined ratios of cumulated Raman signal, R_{tot}, to cumulated fluorescence signal, F_{tot} (detailed in Fig. 11). Results from this analysis suggest that the ratio is optimized ($R_{tot}/F_{tot} > 1$) at gating windows of 4 to 12 ns (Fig. 11D, H) where the amount of Raman signal is maximized relative to fluorescence signal collected. To build on this result, future studies could systematically quantify fluorescence reduction as a function of gate width to optimize development of laboratory or rover-based time-gated Raman systems.

Based on these analyses, and building on previous successes of UV-TG Raman detections of simple synthetic organics (Eshelman *et al*., 2014, 2015), we conclude that both gating and UV λ_{ex} independently reduced fluorescence in our samples containing natural kerogen. Either (or both) strategies could enhance the potential of Raman spectroscopy to detect kerogen in similar lithologies likely to be targeted for analysis on Mars.

4.3. Sample-specific issue with UV Raman spectroscopy

The final goal of this study was to identify sample-specific issues, with UV Raman spectroscopy, that could challenge identifications and affect sample caching. One such issue arose with the evaporitic mudstone.

In the mudstone, visible CW Raman analyses of the matrix and kerogen were impeded by high fluorescence (Fig. 8D, spectrum 1). However, with UV-TG Raman spectroscopy, we did not observe significant fluorescence $<2000\,cm^{-1}$ (Fig. 9 spectrum 10). In this sample, no matrix mineral or organic vibrational bands were detected with UV-TG Raman spectroscopy. (It is notable that at least a weak G band was detectable in all other sample spectra, even when kerogen was not targeted.)

We hypothesize that the absence of Raman information in the mudstone is attributable to strong UV absorption near $\lambda_{ex} = 266$ nm by transition metal (Fe in this sample) coordination complexes. The mudstone contains Fe-bearing phases, as suggested by microscopy (Fig. 8C) and confirmed by visible Raman spectroscopy (hematite, Fig. 8D, spectrum 2) and other techniques (Fe-rich saponite; Table 1). Such minerals commonly exhibit intense and broad charge transfer absorptions between 200 and 300 nm, especially around 240–260 nm (*e.g.*, octahedrally coordinated Fe^{3+} transitions in hematite; Cloutis *et al*., 2008 and references therein).

UV absorption can occur in such phases even at abundances as low as 0.01% by weight (Cloutis *et al*., 2008). Our XRD analyses did not identify Fe oxides, suggesting that crystalline Fe-bearing phases (*e.g.*, hematite) were present below the detection limit of ~5% and that any other Fe phases were likely amorphous. Qualitative microscopy and visible Raman data on the evaporitic mudstone suggest that abundances of Fe-bearing phases were >0.01 bulk wt %.

In contrast, UV absorption did not hamper the identification of spectral features of the marine sandstone, although this sample contains glauconite and illite as possible Fe-bearing phases (Table 1). Perhaps this is due to different distributions and types of such phases in the sandstone, or to differences in Raman scattering cross-sections (Stopar *et al*., 2005).

4.4. Implications for Mars 2020

How does our study inform Mars 2020 rover interpretations? SHERLOC's UV Raman spectrometer is slated to have a range from 810 to >3600 cm^{-1}. This would make it suitable to detect the common diagnostic Raman bands associated with aromatic carbonaceous compounds, if detected on Mars, such as kerogen (D and G bands), including weaker second-order features at 2400–3300 cm^{-1}. However, SHERLOC will not be gated; thus our short-gated spectra (Fig. 9A–C gray spectra) are not directly analogous to what this instrument might observe on Mars. Our long-gated UV Raman results (Fig. 9B, C, black spectra), which mimic UV Raman ungated acquisitions, suggest that an ungated Raman spectrometer is suitable to detect kerogen, if detected on Mars.

Similarly, SHERLOC's fluorescence spectrometer will also be ungated and have a range from 250 to 360 nm. In our data, this region has been indicated in the gray zones in Fig. 10. Observing long-gated fluorescence spectra in our data (black spectra in Fig. 10) within these gray zones, we concluded that SHERLOC's fluorescence spectrometer would allow the UV edge of Type 1 fluorescence features to be visible, if detected. SHERLOC-like fluorescence spectroscopy systems have previously demonstrated UV edge detections of pure organic compounds (*e.g.*, nucleic acids, and aromatics such as phenanthrene; Beegle *et al*., 2014; Beegle *et al*., 2015). In addition, SuperCam's fluorescence spectrometer may provide complementary information about the same features (in different excitation and emission ranges).

Success in identifying potential biosignatures on Mars will be enhanced by using multiple instruments that provide combined data sets at multiple spatial scales, within a well-defined geological context. Microscale imaging for geological context should be provided by Mars 2020's WATSON or SuperCam imagers, which will have a resolution of ~10 s of μm down to 0.65 μm, comparable with Mars Science Laboratory's MAHLI and ChemCam imagers (Edgett *et al*., 2012; Wiens *et al*., 2014).

These microscale imaging contextual observations, together with the discovery of the Raman and fluorescence features discussed, could provide the strongest evidence for the presence of carbonaceous compounds if found on Mars. Such a discovery would call for further analyses using other payload instruments, and may warrant sample caching. We did not determine the precise composition of the components causing either organic spectral signature. This is consistent with a Mars-based scenario where caching decisions will not require knowledge of organic composition or provenance (such biogenicity analyses in cached samples will be performed on Earth).

In one of our samples, the evaporitic mudstone, our UV Raman analyses did not detect biosignatures or minerals (Fig. 9A spectrum 10). We hypothesized that this was caused by strong UV absorptions from transition metals (like Fe) near the laser's UV excitation wavelength (Section 4.3). Although Fe- and other transition metal-bearing minerals are widespread on Mars, many factors could affect the intensity and wavelength of their UV absorption (Cloutis *et al*., 2008 and references therein). These include the abundances of metals; their oxidation states, ion species, coordination environment, and metal–O covalency; grain size and distribution (as detrital grains, interlayer ions, on weathering rims, etc.). For example, Marshall and Marshall (2015) noted related issues with UV Raman detections of Mars analog sulfates rich in Fe, Cr, and Mn.

The systematic study of UV Raman detections of transition metal-bearing minerals and biosignatures preserved in transition metal-rich matrices remains to be explored. Since SHERLOC will have a λ_{ex} in the range of these absorptions, we recommend a systematic exploration of this topic to understand how it might affect SHERLOC analyses. Such studies should examine how UV Raman detections of kerogen depend on the abundance and distribution of both biosignatures and transition metal phases in the matrix, consider absorption due to scales and mechanisms, and assess how instrument factors (*i.e.*, power density and spot size differences) affect detection.

5. Conclusions

Using $\lambda_{ex} = 266$ nm excitation time-gated (UV-TG) Raman and fluorescence spectroscopy systems, we investigated the identification of kerogen as a potential biosignature and its host mineral matrix in seven diverse natural geological field-collected samples. Our samples represent a broad range of depositional environments and lithologies and are considered high-priority astrobiology targets for Mars. Previous work has shown that Raman and fluorescence spectroscopy techniques can detect pure synthetic organics. Our results build on this to demonstrate the value of deep UV Raman and fluorescence spectroscopies for analyzing a suite of challenging, diverse, and high-priority Mars analog geological samples containing natural, nonextracted kerogen composed of complex mixtures of organic compounds.

We explored the capabilities of UV-TG Raman and fluorescence spectroscopies to detect kerogen as a potential biosignature in our samples. Our UV-TG Raman analyses revealed common diagnostic Raman bands associated with aromatic macromolecular carbonaceous compounds, along

with the main vibrational bands of its preserving mineral matrix, without being impeded by fluorescence <2000 cm^{-1}.

A G band indicative of aromatic carbon was detected in most UV-TG Raman spectra, even when not targeting kerogen. This confirmed the utility of the UV excitation wavelength for biosignature detection, but also demonstrated the potential for complications in sample caching decisions on Mars. The presence of D and/or G bands in Raman spectra on Mars would indicate the presence of either abiotic MMC or biogenic kerogen. Such a finding would indicate a potential biosignature and strongly favor caching for sample return. On Earth, detailed laboratory analyses would then be necessary to thoroughly assess its biogenicity.

UV-TG fluorescence analyses revealed that fluorescence from kerogen is detectable as a broad convolution of features between 300 and 500 nm (Type 1) and distinguishable from other (Type 2) organic fluorescence. Together, these data highlight the value of using colocated UV-TG Raman and fluorescence data sets on microscale targeted spots to strengthen the confidence of potential biosignature detection and inform sample caching decisions, without the need for precise compositional knowledge or the organic source. Such analysis would best be performed on Earth following MSR.

Our samples exhibited diverse levels of laser-induced fluorescence in visible CW Raman spectra, which often challenged identifications. We assessed the effectiveness of time gating and UV laser λ_{ex} to reduce fluorescence in Raman spectra and found that the ability to identify kerogen and reduce fluorescence was enhanced by gating and UV excitation independently. Gate times of 4 to 12 ns maximized the Raman signal relative to fluorescence signals. Time gating enabled the detection of complementary but nonessential Raman bands in minerals and kerogen.

A sample-specific issue was revealed for one sample. In the evaporitic mudstone, UV absorption by certain mineral phases may have prevented the identification of mineral and organic features in UV Raman spectra. Further work is needed to understand how UV absorption by transition metals could challenge UV Raman analysis on Mars.

Overall, our results suggest that Mars 2020's SHERLOC, a combined ungated UV Raman/fluorescence spectrometer, may be suited to identify common diagnostic Raman bands and the UV edge of fluorescence features of complex nonextracted targeted kerogen grains in natural samples. In light of the rapidly approaching Mars 2020 launch, our results are intended to guide strategies for caching decisions. Beyond MSR, these results may inform future development of Raman and fluorescence instruments, guided by sample-dependent and science-driven considerations.

Acknowledgments

This work was supported, in part, by a NASA Astrobiology Institute (NAI) Early Career Collaboration Award, the NASA Mars exploration Program, and the Natural Sciences and Engineering Research Council of Canada (NSERC), and the Postdoctoral Fellowship at Carnegie Institution for Science. The use of facilities within the LeRoy Eyring Center for Solid State Science at Arizona State University is gratefully acknowledged. Emily Matys (MIT) is thanked for prompt assistance providing the kerogen standard. Marc Neveu (NASA HQ/USRA) is thanked for assistance with editing. Andrew Steele (Carnegie Institution for Science) is thanked for very helpful discussion and for assistance with the WITec Raman system. Two anonymous reviewers are thanked for their reviews that greatly improved this article.

Author Disclosure Statement

No competing financial interests exist.

References

Abbey, W.J., Bhartia, R., Beegle, L.W., DeFlores, L., Paez, V., Sijapati, K., Sijapati, S., Williford, K., Tuite, M., and Hug, W. (2017) Deep UV Raman spectroscopy for planetary exploration: the search for in situ organics. *Icarus* 290:201–214.

Allwood, A.C., Walter, M.R., Kamber, B.S., Marshall, C.P., and Burch, I.W. (2006) Stromatolite reef from the Early Archaean era of Australia. *Nature* 441:714–718.

Anderson, R.Y., Dean, W.E., Kirkland, D.W., and Snider, H.I. (1972) Permian Castile varved evaporite sequence, west Texas and New Mexico. *Geol Soc Am Bull* 83:59–86.

Apicella, B., Ciajolo, A., and Tregrossi, A. (2004) Fluorescence spectroscopy of complex aromatic mixtures. *Anal Chem* 76: 2138–2143.

Asher, S.A. (1993) UV resonance Raman spectroscopy for analytical, physical, and biophysical chemistry. *Anal Chem* 65: 201A–210A.

Bartholomew, P.R. (2012) Fluorescence interference in Raman Spectroscopy: will the geoscience community drive the instrument industry? 2012 GSA Annual Meeting in Charlotte.

Bartholomew, P.R. (2014) The role of intensity and instrument sensitivity in Raman mineral identification. [abstract 5087]. In *11th International GeoRaman Conference*, St. Louis, MO.

Beegle, L., Bhartia, R., DeFlores, L., Miller, E., Pollack, R., Abbey, W., and Carrier, B. (2016) SHERLOC: on the road to Mars. *LPI Contributions* 1980.

Beegle, L., Bhartia, R., White, M., DeFlores, L., Abbey, W., Wu, Y.-H., Cameron, B., Moore, J., Fries, M., and Burton, A. (2015) SHERLOC: scanning habitable environments with Raman & luminescence for organics & chemicals. In *Aerospace Conference, 2015 IEEE*. IEEE, Big Sky, MT.

Beegle, L.W., Bhartia, R., DeFlores, L., Darrach, M., Kidd, R.D., Abbey, W., Asher, S., Burton, A., Clegg, S., and Conrad, P.G. (2014) SHERLOC: scanning habitable environments with Raman and luminescence for organics and chemicals, an investigation for 2020. *LPI Contributions* 1783:5101.

Bell, E.A., Boehnke, P., Harrison, T.M., and Mao, W.L. (2015) Potentially biogenic carbon preserved in a 4.1 billion-year-old zircon. *Proc Natl Acad Sci* 112:14518–14521.

Bibring, J.P., Langevin, Y., Mustard, J.F., Poulet, F., Arvidson, R., Gendrin, A., Gondet, B., Mangold, N., Pinet, P., Forget, F., Berthé, M., Bibring, J.P., Gendrin, A., Gomez, C., Gondet, B., Jouglet, D., Poulet, F., Soufflot, A., Vincendon, M., Combes, M., Drossart, P., Encrenaz, T., Fouchet, T., Merchiorri, R., Belluci, G., Altieri, F., Formisano, V., Capaccioni, F., Cerroni, P., Coradini, A., Fonti, S., Korablev, O., Kottsov, V., Ignatiev, N., Moroz, V., Titov, D., Zasova, L., Loiseau, D., Mangold, N., Pinet, P., Douté, S., Schmitt, B., Sotin, C., Hauber, E., Hoffmann, H., Jaumann, R., Keller, U., Arvidson, R., Mustard, J.F., Duxbury, T., Forget, F., Neukum, G. (2006) Global mineralogical and aqueous mars history derived from OMEGA/Mars Express data. *Science* 312:400–404.

Bost, N., Ramboz, C., Lebreton, N., Foucher, F., Lopez-Reyes, G., De Angelis, S., Josset, M., Venegas, G., Sanz-Arranz, A., and Rull, F. (2015) Testing the ability of the ExoMars 2018

payload to document geological context and potential habitability on Mars. *Planet Space Sci* 108:87–97.

Bower, D., Steele, A., Fries, M., Green, O., and Lindsay, J. (2016) Raman imaging spectroscopy of a putative microfossil from the ~3.46 Ga Apex chert: insights from quartz grain orientation. *Astrobiology* 16:169–180.

Bower, D., Steele, A., Fries, M., and Kater, L. (2013) Micro Raman spectroscopy of carbonaceous material in microfossils and meteorites: improving a method for life detection. *Astrobiology* 13:103–113.

Bozlee, B.J., Misra, A.K., Sharma, S.K., and Ingram, M. (2005) Remote Raman and fluorescence studies of mineral samples. *Spectrochim Acta A Mol Biomol Spectrosc* 61:2342–2348.

Brasier, M.D., Green, O.R., Jephcoat, A.P., Kleppe, A.K., Van Kranendonk, M.J., Lindsay, J.F., Steele, A., and Grassineau, N.V. (2002) Questioning the evidence for Earth's oldest fossils. *Nature* 416:76–81.

Bressler, S.L., and Butler, R.F. (1978) Magnetostratigraphy of the late Tertiary Verde Formation, central Arizona. *Earth Planet Sci Lett* 38:319–330.

Bridges, J., and Grady, M. (2000) Evaporite mineral assemblages in the nakhlite (martian) meteorites. *Earth Planet Sci Lett* 176:267–279.

Bridges, J.C., Catling, D.C., Saxton, J.M., Swindle, T.D., Lyon, I.C., and Grady, M.M. (2001) Alteration assemblages in Martian meteorites: implications for near-surface processes. *Space Sci Rev* 96(1–4):365–392.

Bristow, T.F., Bish, D.L., Vaniman, D.T., Morris, R.V., Blake, D.F., Grotzinger, J.P., Rampe, E.B., Crisp, J.A., Achilles, C.N., and Ming, D.W. (2015) The origin and implications of clay minerals from Yellowknife Bay, Gale crater, Mars. *Am Mineral* 100:824–836.

Clegg, S.M., Wiens, R.C., Maurice, S., Gasnault, O., Sharma, S.K., Misra, A.K., Newell, R., Forni, O., Lasue, J., and Anderson, R.B. (2015) Remote geochemical and mineralogical analysis with supercam for the Mars 2020 rover. [Abstr] In *Lunar and Planetary Science Conference*.

Cloutis, E.A., McCormack, K.A., Bell, J.F., Hendrix, A.R., Bailey, D.T., Craig, M.A., Mertzman, S.A., Robinson, M.S., and Riner, M.A. (2008) Ultraviolet spectral reflectance properties of common planetary minerals. *Icarus* 197:321–347.

Czaja, A.D., Kudryavtsev, A.B., Cody, G.D., and Schopf, J.W. (2009) Characterization of permineralized kerogen from an Eocene fossil fern. *Org Geochem* 40:353–364.

Des Marais, D.J., Nuth Iii, J.A., Allamandola, L.J., Boss, A.P., Farmer, J.D., Hoehler, T.M., Jakosky, B.M., Meadows, V.S., Pohorille, A., and Runnegar, B. (2008) The NASA astrobiology roadmap. *Astrobiology* 8:715–730.

Desborough, G.A. (1978) A biogenic-chemical stratified lake model for the origin of oil shale of the Green River Formation: an alternative to the playa-lake model. *Geol Soc Am Bull* 89:961–971.

Dickensheets, D.L., Wynn-Williams, D.D., Edwards, H.G.M., Schoen, C., Crowder, C., and Newton, E.M. (2000) A novel miniature confocal microscope/Raman spectrometer system for biomolecular analysis on future Mars missions after Antarctic trials. *J Raman Spectrosc* 31:633–635.

Downs, R.T. (2006) The RRUFF Project: an integrated study of the chemistry, crystallography, Raman and infrared spectroscopy of minerals. In *Program and Abstracts of the 19th General Meeting of the International Mineralogical Association,* (Vol. 3, p. 13), Kobe, Japan.

Edgett, K.S., Yingst, R.A., Ravine, M.A., Caplinger, M.A., Maki, J.N., Ghaemi, F.T., Schaffner, J.A., Bell, J.F., Edwards, L.J., and Herkenhoff, K.E. (2012) Curiosity's Mars hand lens imager (MAHLI) investigation. *Space Sci Rev* 170:259–317.

Ehlmann, B.L., Mustard, J.F., Fassett, C.I., Schon, S.C., Head Iii, J.W., Des Marais, D.J., Grant, J.A., and Murchie, S.L. (2008a) Clay minerals in delta deposits and organic preservation potential on Mars. *Nat Geosci* 1:355–358.

Ehlmann, B.L., Mustard, J.F., Murchie, S.L., Poulet, F., Bishop, J.L., Brown, A.J., Calvin, W.M., Clark, R.N., Marais, D.J., Milliken, R.E., Roach, L.H., Roush, T.L., Swayze, G.A., Wray, J.J. (2008b) Orbital identification of carbonate-bearing rocks on Mars. *Science* 322:1828–1832.

Eneva, M., Falorni, G., Teplow, W., Morgan, J., Rhodes, G., and Adams, D. (2011) Surface deformation at the San Emidio geothermal field, Nevada, from satellite radar interferometry. *Geoth Resour Counc Trans* 35:1647–1653.

Eshelman, E., Daly, M.G., Slater, G., and Cloutis, E. (2015) Time-resolved detection of aromatic compounds on planetary surfaces by ultraviolet laser induced fluorescence and Raman spectroscopy. *Planet Space Sci* 119: 200–207.

Eshelman, E., Daly, M.G., Slater, G., Dietrich, P., and Gravel, J.F. (2014) An ultraviolet Raman wavelength for the in-situ analysis of organic compounds relevant to astrobiology. *Planet Space Sci* 93:65–70.

Farmer, J.D. (2012) Science priorities for Mars astrobiology [abstract 4304]. In *LPI Contributions 1679: Concepts and Approaches for Mars Exploration*.

Farmer, J.D., and Des Marais, D.J. (1999) Exploring for a record of ancient Martian life. *J Geophys Res Planets (1991–2012)* 104:26977–26995.

Ferrari, A.C., and Robertson, J. (2001) Resonant Raman spectroscopy of disordered, amorphous, and diamondlike carbon. *Phys Rev B* 64:075414.

Ferrari, A.C., and Robertson, J. (2004) Raman spectroscopy of amorphous, nanostructured, diamond-like carbon, and nanodiamond. *Philos Trans R Soc Lond A Math Phys Eng Sci* 362: 2477–2512.

Fries, M., and Steele, A. (2010) Raman spectroscopy and confocal Raman imaging in mineralogy and petrography. In *Confocal Raman Microscopy,* edited by Thomas Dieing, *et al.*, Springer, Berlin, 2010.

Frosch, T., Tarcea, N., Schmitt, M., Thiele, H., Langenhorst, F., and Popp, J. (2007) UV Raman imaging a promising tool for astrobiology: comparative Raman studies with different excitation wavelengths on SNC Martian meteorites. *Anal Chem* 79:1101–1108.

Gaft, M., and Nagli, L. (2009) Gated Raman spectroscopy: potential for fundamental and applied mineralogy. *Eur J Mineral* 21:33–42.

Glotch, T.D., and Rogers, A.D. (2007) Evidence for aqueous deposition of hematite-and sulfate-rich light-toned layered deposits in Aureum and Iani Chaos, Mars. *J Geophys Res Planets* 112. E06001.

Glotch, T.D., Bandfield, J.L., Christensen, P.R., Calvin, W.M., McLennan, S.M., Clark, B.C., Rogers, A.D., and Squyres, S.W. (2006) Mineralogy of the light-toned outcrop at Meridiani Planum as seen by the Miniature Thermal Emission Spectrometer and implications for its formation. *J Geophys Res Planets* 111 (E12), doi: 10.1029/2005JE002672.

Gorevan, S.P., Myrick, T., Davis, K., Chau, J.J., Bartlett, P., Mukherjee, S., Anderson, R., Squyres, S.W., Arvidson, R.E., and Madsen, M.B. (2003) Rock abrasion tool: Mars exploration rover mission. *J Geophys Res Planets* 108 (E12), 8068, doi: 10.1029/2003JE002061.

Hofmann, H.J., Grey, K., Hickman, A.H., and Thorpe, R.I. (1999) Origin of 3.45 Ga coniform stromatolites in Warrawoona group, Western Australia. *Geol Soc Am Bull* 111:1256–1262.

Hug, W.F., Bhartia, R., Taspin, A., Lane, A., Conrad, P., Sijapati, K., and Reid, R.D. (2005) Status of miniature integrated UV resonance fluorescence and Raman sensors for detection and identification of biochemical warfare agents. *Opt East* 2005:59940J-59940J-12.

Jehlicka, J., Edwards, H.G., and Culka, A. (2010) Using portable Raman spectrometers for the identification of organic compounds at low temperatures and high altitudes: exobiological applications. *Philos Trans R Soc A* 368:3109–3125.

Jorge-Villar, S.E., and Edwards, H.G.M. (2013) Microorganism response to stressed terrestrial environments: a Raman spectroscopic perspective of extremophilic life strategies. *Life* 3: 276–294.

Lowe, D.R. (1980) Stromatolites 3,400-myr old from the archean of Western Australia. *Nature* 284:441–443.

Madden, M.E.E., Bodnar, R.J., and Rimstidt, J.D. (2004) Jarosite as an indicator of water-limited chemical weathering on Mars. *Nature* 431:821–823.

Maeda, H., Tanaka, G., Shimobayashi, N., Ohno, T., and Matsuoka, H. (2011) Cambrian Orsten Lagerstätte from the Alum Shale Formation: fecal pellets as a probable source of phosphorus preservation. *Palaios* 26:225–231.

Marshall, C.P., Carter, E.A., Leuko, S., and Javaux, E.J. (2006) Vibrational spectroscopy of extant and fossil microbes: relevance for the astrobiological exploration of Mars. *Vib Spectrosc* 41:182–189.

Marshall, C.P., Edwards, H.G.M., and Jehlicka, J. (2010) Understanding the application of Raman spectroscopy to the detection of traces of life. *Astrobiology* 10:229–243.

Marshall, C.P., Emry, J.R., and Marshall, A.O. (2011) Haematite pseudomicrofossils present in the 3.5-billion-year-old Apex Chert. *Nat Geosci* 4:240–243.

Marshall, C.P., and Marshall, A.O. (2015) Challenges analyzing gypsum on Mars by Raman spectroscopy. *Astrobiology 15*: 761–769.

Martyshkin, D.V., Ahuja, R.C., Kudriavtsev, A., and Mirov, S.B. (2004) Effective suppression of fluorescence light in Raman measurements using ultrafast time gated charge coupled device camera. *Rev Sci Instrum* 75:630–635.

McIlreath, I.A., and Morrow, D.W. (1990) *Diagenesis*. Geological Association of Canada.

Misra, A.K., Acosta-Maeda, T.E., Sharma, S.K., McKay, C.P., Gasda, P.J., Taylor, G.J., Lucey, P.G., Flynn, L., Abedin, M.N., and Clegg, S.M. (2016) ''Standoff biofinder'' for fast, noncontact, nondestructive, large-area detection of biological materials for planetary exploration. *Astrobiology* 16:715–729.

Moore, J.N. (1979) Geology map of the San Emidio, Nevada geothermal area (No. DOE/ET/28392-33). University of Utah Research Institute, Earth Science Laboratory, Salt Lake City (USA).

Morris, R.V., Ruff, S.W., Gellert, R., Ming, D.W., Arvidson, R.E., Clark, B.C., Golden, D.C., Siebach, K., Klingelhofer, G., Schroder, C., Fleischer, I., Yen, A.S., Squyres, S.W. (2010) Identification of carbonate-rich outcrops on Mars by the Spirit rover. *Science* 329:421–424.

Morris, R.V., Vaniman, D.T., Blake, D.F., Gellert, R., Chipera, S.J., Rampe, E.B., Ming, D.W., Morrison, S.M., Downs, R.T., and Treiman, A.H. (2016) Silicic volcanism on Mars evidenced by tridymite in high-SiO2 sedimentary rock at Gale crater. *Proc Natl Acad Sci* 201607098.

Muller, K., Waloszek, D., and Maas, A. (2009) *Fossils and Strata, Morphology, Ontogeny and Phylogeny of the Phosphatocopina (Crustacea) from the Upper Cambrian Orsten of Sweden.* John Wiley & Sons.

Mustard, J.F., Adler, M., Allwood, A., Bass, D.S., Beaty, D.W., Bell Iii, J.F., Brinckerhoff, W.B., Carr, M., Des Marais, D.J., and Drake, B. (2013) *Report of the Mars 2020 Science Definition Team, 154 pp., posted July, 2013, by the Mars Exploration Program Analysis Group (MEPAG).* Available online at https://mars.nasa.gov/mars2020/files/mars2020/SDT-Report Finalv6.pdf.

National Research Council, NRC. (2011) *Vision and Voyages: For Planetary Science in the Decade 2013–2022.* National Academies Press, Washington, DC.

Nations, J.D., Hevly, R.H., Blinn, D.W., and Landye, J.J. (1981) *Paleontology, paleoecology, and depositional history of the Miocene-Pliocene Verde Formation, vol 13.* Arizona Geological Society Digest, Yavapai County, Arizona, pp 133–149.

Neuweiler, F., d'Orazio, V., Immenhauser, A., Geipel, G., Heise, K.-H., Cocozza, C., and Miano, T.M. (2003) Fulvic acid–like organic compounds control nucleation of marine calcite under suboxic conditions. *Geology* 31:681–684.

Noe Dobrea, E.Z., Wray, J.J., Calef, F.J., Parker, T.J., and Murchie, S.L. (2012) Hydrated minerals on Endeavour Crater's rim and interior, and surrounding plains: new insights from CRISM data. *Geophys Res Lett* 39. L23201.

Osborne, R.H., Licari, G.R., and Link, M.H. (1982) Modern lacustrine stromatolites, Walker Lake, Nevada. *Sediment Geol* 32:39–61.

Papineau, D., De Gregorio, B., Cody, G., O'Neil, J., Steele, A., Stroud, R., and Fogel, M. (2011) Young poorly crystalline graphite in the >3.8-Gyr-old Nuvvuagittuq banded iron formation. *Nat Geosci* 4:376–379.

Pasteris, J.D., and Wopenka, B. (2003) Necessary, but not sufficient: Raman identification of disordered carbon as a signature of ancient life. *Astrobiology* 3:727–738.

Popa, R., Kinkle, B.K., and Badescu, A. (2004) Pyrite framboids as biomarkers for iron-sulfur systems. *Geomicrobiol J* 21:193–206.

Ray, M.D., Sedlacek, A.J., and Wu, M. (2000) Ultraviolet mini-Raman lidar for stand-off, in situ identification of chemical surface contaminants. *Rev Sci Instrum* 71:3485–3489.

Ruff, S.W., Farmer, J.D., Calvin, W.M., Herkenhoff, K.E., Johnson, J.R., Morris, R.V., Rice, M.S., Arvidson, R.E., Bell, J.F., and Christensen, P.R. (2011) Characteristics, distribution, origin, and significance of opaline silica observed by the Spirit rover in Gusev crater, Mars. *J Geophys Res Planets (1991–2012)* 116, E00F23, doi: 10.1029/2010JE003767.

Scholle, P.A., Ulmer, D.S., and Melim, L.A. (1992) Late-stage calcites in the Permian Capitan Formation and its equivalents, Delaware Basin margin, west Texas and New Mexico: evidence for replacement of precursor evaporites. *Sedimentology* 39:207–234.

Schopf, J.W., Farmer, J.D., Foster, I.S., Kudryavtsev, A.B., Gallardo, V.A., and Espinoza, C. (2012) Gypsum-permineralized microfossils and their relevance to the search for life on Mars. *Astrobiology* 12:619–633.

Schopf, J.W., Kudryavtsev, A.B., Agresti, D.G., Wdowiak, T.J., and Czaja, A.D. (2002) Laser-Raman imagery of Earth's earliest fossils. *Nature* 416:73–76.

Sharma, S.K., Lucey, P.G., Ghosh, M., Hubble, H.W., and Horton, K.A. (2003) Stand-off Raman spectroscopic detection of minerals on planetary surfaces. *Spectrochim Acta A Mol Biomol Spectrosc* 59:2391–2407.

Shreve, A.P., Cherepy, N.J., and Mathies, R.A. (1992) Effective rejection of fluorescence interference in Raman spectroscopy using a shifted excitation difference technique. *Appl Spectrosc* 46:707–711.

Sierra, M.D.S., Donard, O., Lamotte, M., Belin, C., and Ewald, M. (1994) Fluorescence spectroscopy of coastal and marine waters. *Mar Chem* 47:127–144.

Skok, J.R., Mustard, J.F., Ehlmann, B.L., Milliken, R.E., and Murchie, S.L. (2010) Silica deposits in the Nili Patera caldera on the Syrtis Major volcanic complex on Mars. *Nature Geosci* 3:838–841.

Skulinova, M., Lefebvre, C., Sobron, P., Eshelman, E., Daly, M., Gravel, J.F., Cormier, J.F., Châteauneuf, F., Slater, G., and Zheng, W. (2014) Time-resolved stand-off UV-Raman spectroscopy for planetary exploration. *Planet Space Sci* 92:88–100.

Smith, H.D., McKay, C.P., Duncan, A.G., Sims, R.C., Anderson, A.J., and Grossl, P.R. (2014) An instrument design for non-contact detection of biomolecules and minerals on Mars using fluorescence. *J Biol Eng* 8:16.

Socrates, G. (2004) *Infrared and Raman Characteristic Group Frequencies: Tables and Charts*. John Wiley & Sons, West Sussex.

Squyres, S.W., Arvidson, R.E., Bell, J.F., 3rd, Calef, F., 3rd, Clark, B.C., Cohen, B.A., Crumpler, L.A., de Souza, P.A., Jr., Farrand, W.H., Gellert, R., Grant, J., Herkenhoff, K.E., Hurowitz, J.A., Johnson, J.R., Jolliff, B.L., Knoll, A.H., Li, R., McLennan, S.M., Ming, D.W., Mittlefehldt, D.W., Parker, T.J., Paulsen, G., Rice, M.S., Ruff, S.W., Schröder, C., Yen, A.S., Zacny. K. (2012) Ancient impact and aqueous processes at Endeavour Crater, Mars. *Science* 336:570–576.

Squyres, S.W., Grotzinger, J.P., Arvidson, R.E., Bell, J.F., 3rd, Calvin, W., Christensen, P.R., Clark, B.C., Crisp, J.A., Farrand, W.H., Herkenhoff, K.E., Johnson, J.R., Klingelhöfer, G., Knoll, A.H., McLennan, S.M., McSween, H.Y., Jr., Morris, R.V., Rice, J.W., Jr., Rieder, R., Soderblom, L.A. (2004) In situ evidence for an ancient aqueous environment at Meridiani Planum, Mars. *Science* 306:1709–1714.

Steele, A., Fries, M., Amundsen, H., Mysen, B., Fogel, M., Schweizer, M., and Boctor, N. (2007) Comprehensive imaging and Raman spectroscopy of carbonate globules from Martian meteorite ALH 84001 and a terrestrial analogue from Svalbard. *Meteorit Planet Sci* 42:1549–1566.

Steele, A., McCubbin, F., Fries, M., Kater, L., Boctor, N., Fogel, M., Conrad, P., Glamoclija, M., Spencer, M., and Morrow, A. (2012a) A reduced organic carbon component in martian basalts. *Science* 337:212–215.

Steele, A., McCubbin, F.M., and Fries, M.D. (2016) The provenance, formation, and implications of reduced carbon phases in Martian meteorites. *Meteorit Planet Sci* 51:2203–2225.

Steele, A., McCubbin, F.M., Fries, M.D., Golden, D., Ming, D.W., and Benning, L.G. (2012b) Graphite in the martian meteorite Allan Hills 84001. *Am Mineral* 97:1256–1259.

Stopar, J.D., Lucey, P.G., Sharma, S.K., Misra, A.K., Taylor, G.J., and Hubble, H.W. (2005) Raman efficiencies of natural rocks and minerals: performance of a remote Raman system for planetary exploration at a distance of 10 meters. *Spectrochim Acta A Mol Biomol Spectrosc* 61:2315–2323.

Storrie-Lombardi, M.C., Hug, W.F., McDonald, G.D., Tsapin, A.I., and Nealson, K.H. (2001) Hollow cathode ion lasers for deep ultraviolet Raman spectroscopy and fluorescence imaging. *Rev Sci Instrum* 72:4452–4459.

Surdam, R.C., and Stanley, K.O. (1979) Lacustrine sedimentation during the culminating phase of Eocene lake Gosiute, Wyoming (Green River Formation). *Geol Soc Am Bull* 90:93–110.

Tarcea, N., Harz, M., Rösch, P., Frosch, T., Schmitt, M., Thiele, H., Hochleitner, R., and Popp, J. (2007) UV Raman spectroscopy—a technique for biological and mineralogical in situ planetary studies. *Spectrochim Acta A Mol Biomol Spectrosc* 68:1029–1035.

Van Beynen, P., Bourbonniere, R., Ford, D., and Schwarcz, H. (2001) Causes of colour and fluorescence in speleothems. *Chem Geol* 175:319–341.

Van Kranendonk, M.J., Webb, G.E., and Kamber, B.S. (2003) Geological and trace element evidence for a marine sedimentary environment of deposition and biogenicity of 3.45 Ga stromatolitic carbonates in the Pilbara Craton, and support for a reducing Archaean ocean. *Geobiology* 1:91–108.

Vandenbroucke, M., and Largeau, C. (2007) Kerogen origin, evolution and structure. *Org Geochem* 38:719–833.

Vaniman, D.T., Bish, D.L., Ming, D.W., Bristow, T.F., Morris, R.V., Blake, D.F., Chipera, S.J., Morrison, S.M., Treiman, A.H., Rampe, E.B., Rice, M., Achilles, C.N., Grotzinger, J.P., McLennan, S.M., Williams, J., Bell, J.F., 3rd, Newsom, H.E., Downs, R.T., Maurice, S., Sarrazin, P., Yen, A.S., Morookian, J.M., Farmer, J.D., Stack, K., Milliken, R.E., Ehlmann, B.L., Sumner, D.Y., Berger, G., Crisp, J.A., Hurowitz, J.A., Anderson, R., Des Marais, D.J., Stolper, E.M., Edgett, K.S., Gupta, S., Spanovich, N.; MSL Science Team. (2014) Mineralogy of a mudstone at Yellowknife Bay, Gale crater, Mars. *Science* 343:1243480.

Wadell, J. (1972) Sedimentation and stratigraphy of the Verde Formation (Pliocene). Master's Thesis, Tempe, Arizona, ASU.

Wang, A., Freeman, J.J., Jolliff, B.L., and Chou, I.M. (2006) Sulfates on Mars: a systematic Raman spectroscopic study of hydration states of magnesium sulfates. *Geochim Cosmochim Acta* 70:6118–6135.

Wiens, R.C., Maurice, S., Johnson, J.R., Clegg, S.M., Sharma, S.K., Rull, F., Montmessin, F., Anderson, R.B., Beyssac, O., Bonal, L., and Deflores, L. (2014) The SuperCam remote sensing suite for Mars 2020: co-aligned LIBS, Raman, and near-IR spectroscopies, and color micro-imaging [abstract 1086]. In *International Workshop on Instrumentation for Planetary Missions (IPM-2014),* NASA Goddard Space Flight Center, Greenbelt, MD.

Wood, J.D. (1991) Geology of the Wind Mountain gold deposit, Washoe County, Nevada. In: *Geology and Ore Deposits of the Great Basin.* Symposium proceedings: Geological Society of Nevada, Reno.

Address correspondence to:
Svetlana Shkolyar
Geophysical Laboratory
Carnegie Institution for Science
5251 Broad Branch Road NW
Washington, DC 20015

E-mail: sshkolyar@carnegiescience.edu

Submitted 6 July 2017
Accepted 3 November 2017

Abbreviations Used

CRIS = confocal Raman imaging spectroscopy
CW = continuous wave
MMC = macromolecular carbon
MSR = Mars sample return
PAHs = polycyclic aromatic hydrocarbons
UV-TG = UV time-gated
XRPD = X-ray powder diffraction